Computers and Mathematics with Applications 104 (2021) 14–33

Contents lists available at ScienceDirect

Computers and Mathematics with Applications

www.elsevier.com/locate/camwa

A spline-based FE approach to modelling of high frequency dynamics of 1-D structures

A. Żak *, W. Waszkowiak

Gdańsk University of Technology, Faculty of Electrical and Control Engineering, ul. Narutowicza 11/12, 80-234 Gdańsk, Poland

ARTICLE INFO

Keywords:
Splines
Finite elements
Finite element method
High frequency dynamics
Wave propagation

ABSTRACT

In this paper a computational methodology leading to the development of a new class of FEs, based on the application of continuous and smooth approximation polynomials, being splines, has been presented. Application of the splines as appropriately defined piecewise elemental shape functions led the authors to the formulation of a new approach for FEM, named as spFEM, where contrary to the well-known NURBS approach, the boundaries of spFEs are well-defined, exactly as it is in the case of the traditional FEM.

The current approach has been computationally verified by the authors it terms of high frequency dynamics including such problems as: spectra of natural frequencies, modes of natural vibrations as well as wave propagation problems, especially in the aspect of high frequency responses, all in the case of selected problems involving one- and two-mode theories of 1-D structural elements. The applicability of the proposed approach has been evaluated and compared, in terms of calculated dynamic responses, with the results obtained by the use of well-established FEM approaches: classical FEM as well as TD-SFEM.

In all cases investigated by the authors the proposed spFEM approach turned out to be the most accurate approach, free from the main drawback of the other tested FEM approaches thanks to the class of differentiability of approximation polynomials, which guarantees the absence of frequency band gaps in calculated spectra of natural frequencies. A direct consequence of this feature of the proposed approach is that a larger part of the calculated spectra of natural frequency, the same as modes of natural vibrations, can effectively be used for more accurate calculations of dynamic reposes even in the case of multi-mode theories. This in contrast to the other tested FEM approaches.

1. Introduction

Wave propagation problems present a serious computational challenge, especially in the context of damage detection [1]. It should be noted that numerous computational techniques may be used for that purpose, but with no doubts the most popular one remains the finite element method (FEM) [2–4]. As a numerical technique FEM [5–7] is characterised by its great flexibility, which allows researches to analyse various problems not only in complex engineering structures in terms of their geometry (1-D, 2-D and 3-D) and material properties (isotropic, orthotropic or fully anisotropic), but also lends itself to tackling steady-state or transient linear and non-linear problems.

However, the very nature of damage detection by the use of guided elastic waves in engineering structures and by the application of FEM requires that traditional finite element (FE) numerical models must comprise many degrees of freedom (DOFs), reaching millions or even more. Moreover, the characteristic dimensions of FEs must be of the same or lower order than the characteristic dimension of the damage that is modelled, and also must be smaller than the shortest waves that may result from numerical computations. The huge numerical models, associated with such discretisation requirements of computational domains, must fulfil extra conditions of regular mesh shapes in order to prevent the effect of undesired and/or artificial numerical anisotropy. Additionally, it should be pointed out that during numerical computations these huge numerical models must be solved numerically many times (once on each time step during linear analysis and iteratively a number of times on each time step during non-linear analysis) in order to achieve the final solution.

Despite the fact of its indisputable advantages FEM is not free of disadvantages. In the classical FEM the variation of unknown quantities within FEs is described by the use of certain approximation functions, which are known as shape functions. Typically, shape functions are rep-

---

* Corresponding author.
E-mail addresses: arkadiusz.zak@pg.edu.pl (A. Żak), wiktor.waszkowiak@pg.edu.pl (W. Waszkowiak).

https://doi.org/10.1016/j.camwa.2021.11.003
Received 16 April 2021; Received in revised form 12 August 2021; Accepted 4 November 2021

resented by polynomials of certain degrees. In the case of the classical FEM they are approximation polynomials of the first or second degree, while in the case of more specialised FEM approaches (adaptive FEM or the Time-domain Spectral Finite Element Method, TD-SFEM) the degree of approximation polynomials may be as high as six, eight or even higher [8–10]. It should be underlined that in the case of the classical FEM, derivatives of the approximation shape functions remain continuous within FEs, but they are discontinuous between adjacent FEs, which directly leads to the discontinuity of the strain/stress field between these FEs. This feature remains unimportant in static and low frequency dynamic problems solved by FEM. However, in high frequency dynamics involving wave propagation problems, the discontinuity of the stress/strain field between adjacent FEs may lead to numerous numerical issues due to the presence of frequency band gaps in calculated spectra of natural frequencies. Their presence may have a significant impact on the accuracy of numerical results, or which can even lead to false results and observations based on them [11,12]. This may be additionally magnified and exacerbated by the requirement of dense and regular discretisation of computational domains, where discontinuities of approximation polynomials, together with not perfectly smooth geometry, may play a very important role.

Under these circumstances it seems natural to look at such approximation shape functions that could help to minimise all the undesired features of typical FE shape functions previously mentioned. A good candidate for such functions seem spline functions, which are in fact approximation polynomials characterised by continuity and smoothness [13–15]. The most popular technique used here seems the method employing B-spline functions, also knowns as Non-uniform Rational B-splines (NURBS) [16–18]. However, in comparison to FEM, the approaches based on B-splines suffer from one main disadvantage, which is the lack of well-defined elements. They are based on so-called *patches* rather than typical elements, which in FEM are well localised in space. The lack of this feature makes these B-spline approaches rather difficult to adopt directly in the case of various numerical techniques employed in FEM, for example, for damage modelling [19] understood as structural discontinuities or structural joints [20]. Apart from that very often discretisation points within so-called *knot vectors* may posses nodes that stay outside of computational domains [21–23], which additionally makes the discretisation process complex and difficult.

All the modelling features above mentioned, related to the discussed types of computational approaches: FEM, TD-SFEM, B-splines and spFEM, are summarised in Table 1.

Table 1
A concise summary of selected typical modelling features of discussed types of computational approaches.

Feature	FEM	TD-SFEM	B-splines	spFEM
Well-defined elements	yes	yes	no	yes
Continuous displacement fields	yes	yes	yes	yes
Continuous strain/stress fields	no	no	yes	yes
Gapless frequency spectra	no	no	yes	yes
Ease of joint modelling	yes	yes	no	yes
Ease of damage modelling	yes	yes	no	yes

The idea presented in this work is the authors' attempt to combine together the flexibility of FEM, as one of the most popular tools used nowadays in research and engineering practice, with the unquestionable numerical advantages of spline-based approximation, as it is presented in Table 1. In the current paper this is achieved in the following steps. First of all a general method used to obtain appropriate 1-D approximation polynomials is presented, which are spline-based elemental shape functions. Next, the spline-based shape functions are employed to build characteristic elemental stiffness and inertia matrices in the case of one- and two-mode theories of 1-D structural elements. The results of comparative analysis, discussed by the authors, concern high frequency dynamics of rod and beam responses including: spectra of natural frequencies (through the application of the Bloch theorem), modes of natural vibrations, dispersion curves as well as wave propagation. They aim to underline the benefits of the spFEM approach in comparison with three alternative types of computational approaches, mainly: FEM, TD-SFEM and B-splines.

2. Spline-based elemental shape functions

It is very convenient to derive shape functions for a new class of spline-based finite elements (spFEs) starting from a simple case of a 1-D element of length l, defined in the local coordinate system of the element x. In general, it is assumed that the element has 2 nodes. The total number of DOFs in each node is directly dependent on the degree of approximation polynomials used as shape functions: 1 DOF in each node for linear approximation polynomials ($p = 1$), 2 DOFs in each node for quadratic approximation polynomials ($p = 2$), 3 DOFs in each node for cubic approximation polynomials ($p = 3$), etc. It should be noted that in the current formulation nodal DOFs represent not only the unknown function $f(x)$, but also its first and higher-order spatial derivatives.

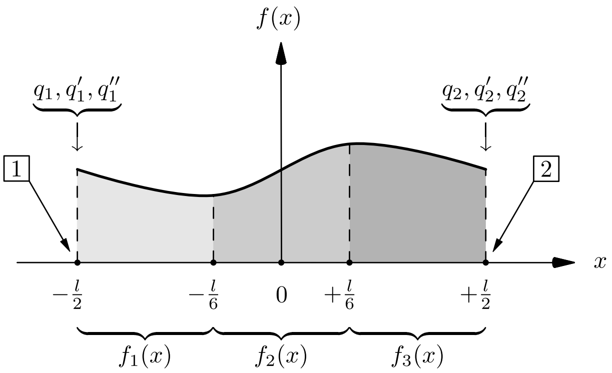

Fig. 1. A concept of a 1-D spline-based finite element (spFE) in the local co-ordinate system x.

A general procedure, directly adopted from FEM, leading to the determination of spline-based elemental shape functions, is presented by the authors in detail for cubic approximation polynomials. This procedure can be easily modified in order to incorporate additional element features like: internal damage in the form of a fatigue crack or a step change in material properties – see Section 5. In the current case the element has 2 nodes and 3 DOFs per node, while nodal DOFs represent values q_1, q_2 of the unknown function $f(x)$ as well as their spatial derivatives in respect of x: first derivatives q_1', q_2' and second derivatives q_1'', q_2''. Additionally, it is assumed that the unknown function $f(x)$ within the element can be expressed by a set of piecewise spline approximation polynomials of degree $p = 3$, as presented in Fig. 1.

The unknown function $f(x)$ can be presented in the local co-ordinate system x in the following form:

$$f(x) = \begin{cases} f_1(x) = a_0 + a_1 x + a_2 x^2 + a_3 x^3, & \text{if } -\frac{l}{2} \le x < -\frac{l}{6} \\ f_2(x) = a_4 + a_5 x + a_6 x^2 + a_7 x^3, & \text{if } -\frac{l}{6} \le x < +\frac{l}{6} \\ f_3(x) = a_8 + a_9 x + a_{10} x^2 + a_{11} x^3, & \text{if } +\frac{l}{6} \le x \le +\frac{l}{2} \end{cases} \tag{1}$$

where $a_0, \ldots, a_{11}$ are 12 unknown coefficients, which can be easily evaluated based on 6 nodal conditions and 6 continuity conditions:

$$\begin{cases} f_1(-\frac{l}{2}) = q_1, & f_1(-\frac{l}{6}) - f_2(-\frac{l}{6}) = 0 \\ f_1'(-\frac{l}{2}) = q_1', & f_1'(-\frac{l}{6}) - f_2'(-\frac{l}{6}) = 0 \\ f_1''(-\frac{l}{2}) = q_1'', & f_1''(-\frac{l}{6}) - f_2''(-\frac{l}{6}) = 0 \\ f_3(+\frac{l}{2}) = q_2, & f_2(+\frac{l}{6}) - f_3(+\frac{l}{6}) = 0 \\ f_3'(+\frac{l}{2}) = q_2', & f_2'(+\frac{l}{6}) - f_3'(+\frac{l}{6}) = 0 \\ f_3''(+\frac{l}{2}) = q_2'', & f_2''(+\frac{l}{6}) - f_3''(+\frac{l}{6}) = 0 \end{cases} \tag{2}$$

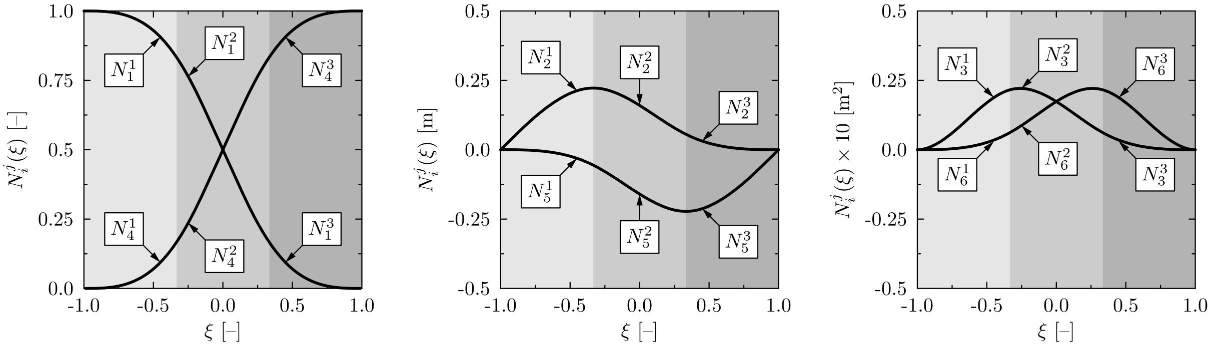

Fig. 2. Piecewise 1-D spline-based elemental shape functions $N_i^j(\xi)$ of degree $p = 3$, associated with nodal DOFs: displacements q_1 and q_2 (left), rotations q_1' and q_2' (middle), rotation derivatives q_1'' and q_2'' (right), in the local normalised co-ordinate system of the element ξ, obtained in the case of the unit element length $l = 1$ m.

These 12 conditions allow one to build a system of algebraic equations in the form of the matrix **A** necessary to find the 12 unknown coefficients $a_0, \ldots, a_{11}$ as:

$$\mathbf{a} = \mathbf{A}^{-1} \cdot \mathbf{b} \tag{3}$$

where the column vectors **a** and **b** have the following forms:

$$\mathbf{a} = \{a_0, \ldots, a_{11}\}^{\intercal}, \quad \mathbf{b} = \{q_1, q_1', q_1'', 0, 0, 0, 0, 0, 0, q_2, q_2', q_2''\}^{\intercal} \tag{4}$$

In the final step, knowing that the 12 coefficients $a_0, \ldots, a_{11}$ are simultaneously dependent on all nodal quantities and their first and second derivatives, after simple mathematical manipulations and rearrangements of terms, piecewise spline-based elemental shape functions $\mathbf{N}(x)$ can be presented as [6]:

$$f(x) = \mathbf{N}(x) \cdot \mathbf{q} \quad \text{or} \quad f(x) = \mathbf{N}(\xi(x)) \cdot \mathbf{q} \tag{5}$$

where the column nodal vector **q** has the form of $\mathbf{q} = \{q_1, q_1', q_1'', q_2, q_2', q_2''\}^{\intercal}$ and where:

$$\mathbf{N}(x) = \begin{cases} \mathbf{N}^1(x), & \text{if } -\frac{l}{2} \le x < -\frac{l}{6} \\ \mathbf{N}^2(x), & \text{if } -\frac{l}{6} \le x < +\frac{l}{6} \\ \mathbf{N}^3(x), & \text{if } +\frac{l}{6} \le x \le +\frac{l}{2} \end{cases} \quad \text{or} \quad \mathbf{N}(\xi) = \begin{cases} \mathbf{N}^1(\xi), & \text{if } -1 \le \xi < -\frac{1}{3} \\ \mathbf{N}^2(\xi), & \text{if } -\frac{1}{3} \le \xi < +\frac{1}{3} \\ \mathbf{N}^3(\xi), & \text{if } +\frac{1}{3} \le \xi \le +1 \end{cases} \tag{6}$$

with a new variable ξ introduced as $\xi = \frac{2}{l}x$.

In fact, such a transformation of variables is equivalent to representation of the element under consideration in a form typical of FEM, in the local normalised co-ordinate system of the element ξ. This greatly helps not only to simplify notation [5–7], but also to simplify all subsequent computations [1] based on the application of the piecewise 1-D spline-based shape functions. As a result it can be written that:

$$\mathbf{N}^1(\xi) = \begin{Bmatrix} +\frac{7}{16} - \frac{27}{16}\xi - \frac{27}{16}\xi^2 - \frac{9}{16}\xi^3 \\ +\frac{l}{8} - \frac{5l}{8}\xi - \frac{9l}{8}\xi^2 - \frac{3l}{8}\xi^3 \\ +\frac{l^2}{96} + \frac{3l^2}{32}\xi + \frac{7l^2}{32}\xi^2 + \frac{11l^2}{96}\xi^3 \\ +\frac{9}{16} + \frac{27}{16}\xi + \frac{27}{16}\xi^2 + \frac{9}{16}\xi^3 \\ -\frac{3l}{16} - \frac{9l}{16}\xi - \frac{9l}{16}\xi^2 - \frac{3l}{16}\xi^3 \\ +\frac{l^2}{48} + \frac{l^2}{16}\xi + \frac{l^2}{16}\xi^2 + \frac{l^2}{48}\xi^3 \end{Bmatrix}^{\intercal}, \quad \text{if} - 1 \le \xi < -\frac{1}{3} \tag{7}$$

$$\mathbf{N}^2(\xi) = \begin{Bmatrix} -\frac{1}{2} - \frac{9}{8}\xi + \frac{9}{8}\xi^3 \\ +\frac{23l}{144} - \frac{5l}{16}\xi - \frac{3l}{16}\xi^2 + \frac{9l}{16}\xi^3 \\ +\frac{5l^2}{288} - \frac{l^2}{32}\xi - \frac{l^2}{32}\xi^2 + \frac{7l^2}{96}\xi^3 \\ +\frac{1}{2} + \frac{9}{8}\xi - \frac{9}{8}\xi^3 \\ -\frac{23l}{144} - \frac{5l}{16}\xi + \frac{3l}{16}\xi^2 + \frac{9l}{16}\xi^3 \\ +\frac{5^2}{288} + \frac{l^2}{32}\xi - \frac{l^2}{32}\xi^2 - \frac{7l^2}{96}\xi^3 \end{Bmatrix}^{\intercal}, \quad \text{if} - \frac{1}{3} \le \xi < +\frac{1}{3} \tag{8}$$

$$\mathbf{N}^3(\xi) = \begin{Bmatrix} +\frac{9}{16} - \frac{27}{16}\xi + \frac{27}{16}\xi^2 - \frac{9}{16}\xi^3 \\ +\frac{3l}{16} - \frac{9l}{16}\xi + \frac{9l}{16}\xi^2 - \frac{3l}{16}\xi^3 \\ +\frac{l^2}{48} - \frac{l^2}{16}\xi + \frac{l^2}{16}\xi^2 - \frac{l^2}{48}\xi^3 \\ +\frac{7}{16} + \frac{27}{16}\xi - \frac{27}{16}\xi^2 + \frac{9}{16}\xi^3 \\ -\frac{l}{8} - \frac{5l}{8}\xi + \frac{9l}{8}\xi^2 - \frac{3l}{8}\xi^3 \\ +\frac{l^2}{96} + \frac{3l^2}{32}\xi + \frac{7l^2}{32}\xi^2 + \frac{11l^2}{96}\xi^3 \end{Bmatrix}^{\intercal}, \quad \text{if} + \frac{1}{3} \le \xi \le +1 \tag{9}$$

The variation of the piecewise 1-D spline-based elemental shape functions $N_i^j(\xi)$, (where $i = 1, \ldots, 6$ and $j = 1, \ldots, 3$), as a function on the non-dimensional variable ξ, is shown in Fig. 2. It is presented for appropriate ranges of the non-dimensional variable ξ, i.e. for $\xi \in \langle -1, -\frac{1}{3} \rangle$, for $\xi \in \langle -\frac{1}{3}, +\frac{1}{3} \rangle$ and for $\xi \in \langle +\frac{1}{3}, +1 \rangle$, as well as assuming the unit length of the element $l = 1$ m.

It can be seen from Fig. 2 that the piecewise 1-D spline-based shape functions of the element $N_i^j(\xi)$ remain continuous and smooth within the element up to their second spatial derivatives. Thus, it can be concluded that the shape functions $N_i^j(\xi)$ belong to the class C^2 of differentiable functions. This is in contrast to the classical FEM or TD-SFEM, where it is only required for 1-D elemental shape functions to remain continuous and therefore such shape functions belong to the class C^0.

Moreover, it is shown in the following paragraphs that a property of 1-D shape functions, understood as the difference between the degree of approximation polynomials p and the degree of their continuity c between adjacent FEs, defined as $d = p - c - 1$, plays a very important role. It turns out that it has a great influence on the quality of computed dynamic responses in the case of high frequency dynamic responses, especially in the context of wave propagation problems. It should be emphasised here that based on the 2 nodes and associated nodal DOFs 1-D Hermite approximation polynomials of degree $p = 5$ could be built, instead of the piecewise 1-D spline-based approximation polynomials of degree $p = 3$. However, it is shown later that the application of Hermite approximation polynomials to high frequency dynamic problems is limited due to some undesired numerical properties, which can be directly associated with the parameter d.

A general procedure described above and employed to determine of the piecewise 1-D spline-based elemental shape functions for cubic approximation polynomials can be directly adopted and used for other degrees of approximation polynomials, such as: linear, quadratic or higher. The result of its application is presented in Fig. 3, where piecewise 1-D spline-based elemental shape functions $N_i^j(\xi)$, associated only with nodal displacement DOFs, are shown for the degrees of approximation polynomials $p = 1$, $p = 2$ as well as $p = 3$.

In order to compare the results obtained with other types of 1-D elemental shape functions already mentioned, similar results to these presented in Fig. 3 were obtained for the classical FEM approach as well as piecewise B-splines. They are presented in Fig. 4 and Fig. 5, respectively and are summarised in Table 2.

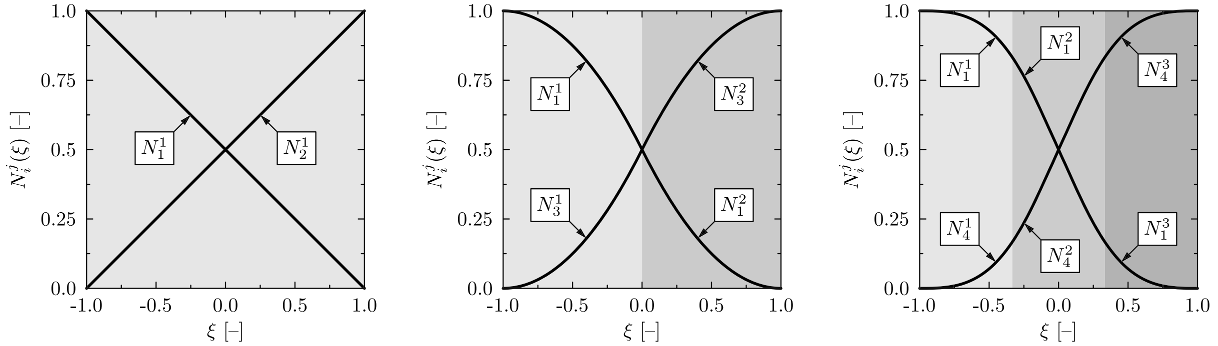

Fig. 3. Piecewise 1-D spline-based elemental shape functions $N_i^j(\xi)$ associated with nodal displacement DOFs for approximation polynomials of degree: $p = 1$ (left), $p = 2$ (middle), $p = 3$ (right), in the local normalised co-ordinate system of the element ξ, obtained in the case of the unit length of the element $l = 1$ m.

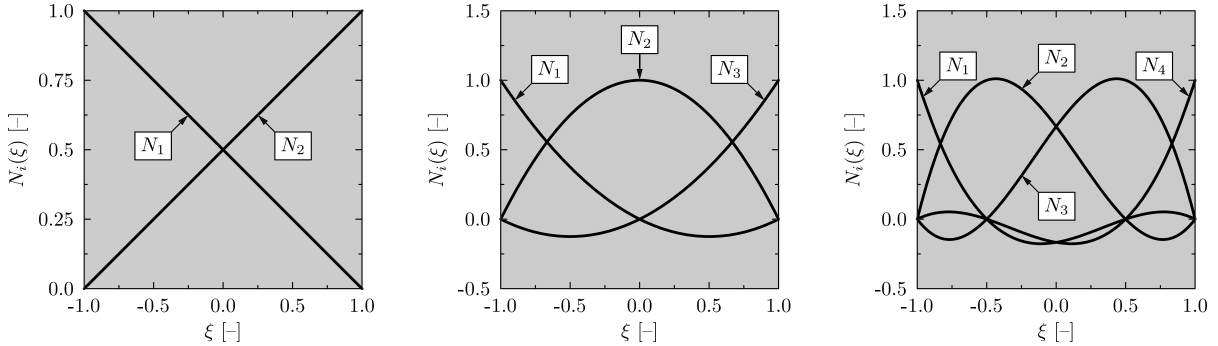

Fig. 4. 1-D classical elemental shape functions $N_i^j(\xi)$ associated with nodal displacement DOFs for approximation polynomials of degree: $p = 1$ (left), $p = 2$ (middle), $p = 3$ (right), in the local normalised co-ordinate system of the element ξ.

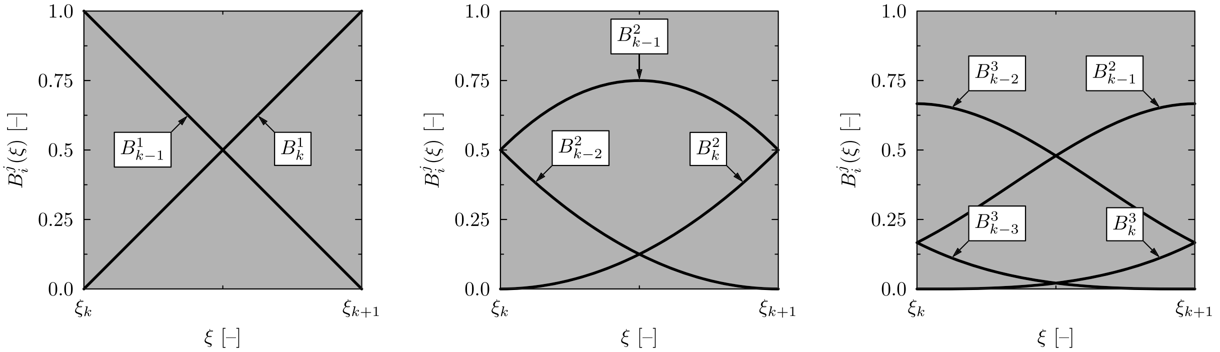

Fig. 5. Piecewise 1-D B-spline elemental shape functions $N_i^j(\xi)$ associated with nodal displacement DOFs for approximation polynomials of degree: $p = 1$ (left), $p = 2$ (middle), $p = 3$ (right), in the local co-ordinate system associated with one knot interval $\xi \in \langle \xi_k, \xi_{k+1} \rangle$.

Table 2
Additional modelling features of discussed types of computational approaches.

Feature	FEM	TD-SFEM	B-splines	spFEM
Local continuity of solution	typically up to C^1	no limit	no limit	typically up to $C^{2\dagger}$
Global continuity of solution	C^0	C^0	$C^{0\ddagger}$	the same as local
Support of approx. polynomials	local	local	several knot intervals	local

† Due to computation complexity.
‡ Depends on boundary conditions.

It can be clearly seen that all three approaches, i.e. spline-based, classical FEM and B-spline are identical in the case of linear approximation polynomials, when $p = 1$, and for higher degrees of approximation polynomials they tend to differ. For quadratic approximation polynomials 1-D elemental shape functions have similar variations in the case of the classical FEM and B-spline approaches, however they change significantly for cubic approximation polynomials. This is not the case for the piecewise 1-D spline-based elemental shape functions, where only slight differences between quadratic and cubic approximation polynomials are visible.

Moreover, it can be noted that in the case of the classical FEM an increase in the degree of approximation polynomials p, used for 1-D elemental shape functions, and based on equidistant distribution of nodes, leads to undesired oscillations of these polynomials close to the element ends [24]. This is well known as Runge's phenomenon and can be avoided only for specialised TD-SFEM node distributions, which are known in the literature as Chebyshev or Lobatto distribution of nodes [1]. For this reason the classical FEM approach is typically based on the use of linear or quadratic elemental shape functions. This problem is not present for the piecewise B-spline elemental shape functions, but this is possible at the additional cost of an increase of B-spline function support onto neighbouring knots. As a consequence the definition of an element, similar to this known in FEM or TD-SFEM, is impossible.

These two problems described above are not present in the current spline-based approach, where an increase in the degree of approximation polynomials p is possible thanks to additional elemental DOFs, which are not explicitly associated with any internal nodal information (extra nodes), as in the case of FEM or TD-SFEM. In contrast, they are associated with spatial derivatives of nodal quantities at two element nodes. This helps not only to avoid Runge's phenomenon, but also allows for keeping the shape function support within one FE.

A much more important property of piecewise 1-D spline-based elemental shape functions is the class of their continuity, which has a direct influence on important features of numerical solutions. It should be said that in FEM or TD-SFEM the class of continuity of 1-D elemental shape functions can be arbitrary, depending only on the number of element nodes, providing the distribution of nodes within FEs is appropriate to avoid Runge's phenomenon. Unfortunately a high class of continuity provided locally on the element level is not maintained globally, since the stress/strain fields between adjacent FEs are discontinuous. This may lead to some undesired properties of FE discrete numerical models such as the presence of frequency band gaps in natural frequency spectra, which on the other hand may significantly influence calculated numerical dynamic responses. This problem should not be present in the case of the B-spline approach. However, due to the type of support typical for B-splines (including several knot intervals) and numerical features of B-splines, multiple knots are used in order to bring approximation functions closer to control points of interpolation at the ends of the region of interest. Such a repetition of knots results in a decrease in the class of continuity at the multiple knots down to the class C^{p-m-1}, where p is the degree of approximation polynomials used in B-splines and m is the knot multiplicity. As a consequence also in this case the same class of continuity of numerical solutions cannot be maintained in the entire region of interest. However, this problem does not exist when the piecewise 1-D spline-based elemental shape functions are employed, where the class of continuity is maintained in the entire region of interest thanks to the use of higher order DOFs at element nodes, which are first and higher-order spatial derivatives.

Such a formulation of the 1-D piecewise spline-based elemental shape functions, as described above, can be easily employed for the definition of 1-D spFEs such as rods and beams. This can be achieved according to the well-known general FEM procedures [5–7], which are commonly used to calculate elemental characteristic stiffness $\mathbf{K}$ and inertia $\mathbf{M}$ matrices:

$$\mathbf{K} = \iiint_V \mathbf{B}^{\mathsf{T}} \cdot \mathbf{D} \cdot \mathbf{B} \, dV, \quad \mathbf{M} = \rho \iiint_V \mathbf{N}^{\mathsf{T}} \cdot \mathbf{N} \, dV \tag{10}$$

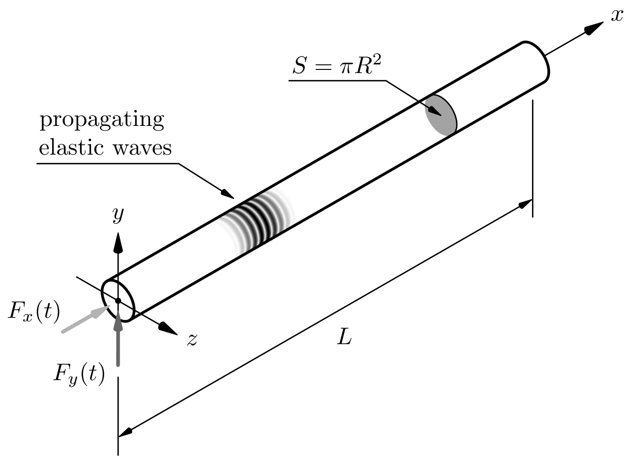

Fig. 6. Geometry of a structural bar element.

where $\mathbf{B} = \mathbf{\Gamma N}$ is known as the matrix of relationships between strains and displacements, $\mathbf{\Gamma}$ denotes a linear differentiation operator, while $\mathbf{D}$ is the matrix of elastic coefficients [1]. Additionally, ρ is material density and V is the FE volume.

The applicability of the 1-D piecewise spline-based elemental shape functions is demonstrated in the following paragraphs of this paper and concerns such dynamic characteristics as natural frequencies and modes vibrations together with wave propagation responses.

3. Periodic properties of FE discrete numerical models

The immanent property of the classical (displacement) formulation of FEM is the discontinuity of the stress/strain fields between adjacent FEs. Because of this, regardless of their finite dimensions and types of boundary conditions or mesh densities, FE discrete numerical models may be considered as representing structures of properties typical to periodic structures. This can be easily observed in the case of 1-D structures, however, for 2-D or 3-D structures the same kind of behaviour may be found, which is reinforced by their higher dimensions. Periodic properties of FE discrete numerical models may manifest themselves in a particularly strong manner in problems involving the analysis of propagation of elastic waves. This is a direct consequence of the fact that this type of analysis requires very dense and very regular meshes of FEs [1].

3.1. Bloch theorem and its consequences

The Bloch theorem in a powerful analytical tool that enables one to investigate the dynamic properties and behaviour of periodic structures [25] in nano-, micro- as well as in macro-scales – see *Appendix A*. Most commonly it is used to study the behaviour of electrons in various crystals, however, its application is much more general. The Bloch theorem can be employed to study wave propagation phenomena in periodic media or structures [11,12,26]. For example, in periodic dielectric materials the Bloch theorem can be used to analyse photonic crystals or in periodic media to analyse phononic crystals [27].

The application of the Bloch reduction technique is demonstrated in the case of investigation of longitudinal modes of natural vibrations of a 1-D periodic bar – see *Appendix B*. For this analysis it was assumed that the bar under investigation presented in Fig. 6, of periodic boundary conditions, has the following geometrical dimensions: length $L = 2000$ mm and radius $R = 20$ mm, as well as the following material properties: elastic modulus $E = 67.5$ GPa, Poisson's ratio $\nu = 0.33$ and material density $\rho = 2700$ kg/m^3.

In this particular case it was additionally assumed that the bar consists of $M = 200$ periodic cells having the length $l = 10$ mm, which are characterised by two different phase velocities: $c_{p|1} = 5$ km/s over the cell length $l_1 = 8$ mm, and $c_{p|2} = 2.5$ km/s over the cell length $l_2 = 2$ mm

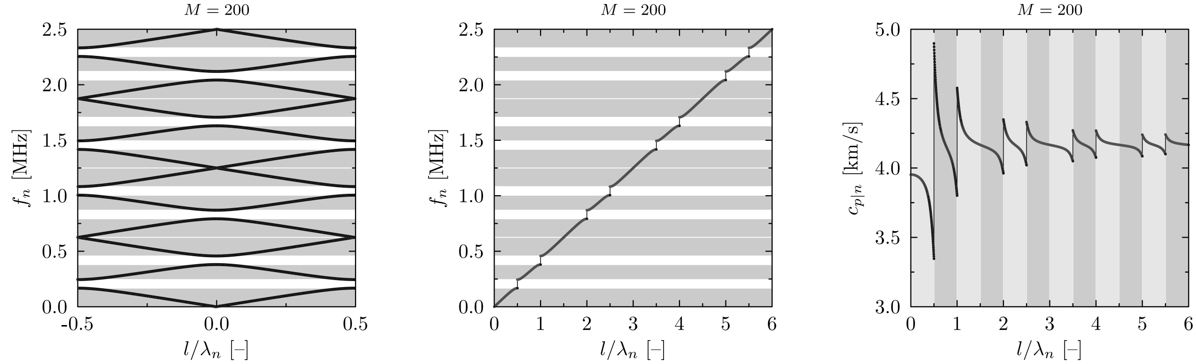

Fig. 7. Natural frequencies f_n of longitudinal modes of natural vibrations of a 1-D periodic bar of step changes in the elastic modulus, consisting $M = 200$ cells, as a function of the ratio l/λ_n: in the reduced zone (left), in the extended zone (middle), with frequency band gaps indicated in white. Analytical solution obtained by the use of the Bloch theorem [25,27]. A resulting dispersion curve for the phase velocity $c_{p|n}$ as a function of the ratio l/λ_n (right).

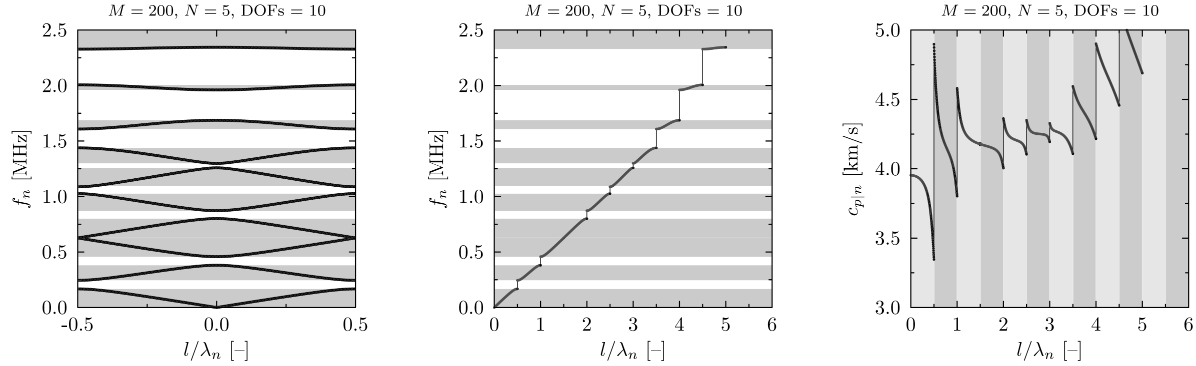

Fig. 8. Natural frequencies f_n of longitudinal modes of natural vibrations of a 1-D periodic bar of step changes in the elastic modulus, consisting $M = 200$ cells, as a function of the ratio l/λ_n: in the reduced zone (left), in the extended zone (middle), with frequency band gaps indicated in white. Numerical results obtained by the use of Bloch reduction [29] and spFEM, according to the classical rod theory, for a unit cell modelled by 5 rod spFEs and approximation polynomials of degree $p = 2$. A resulting dispersion curve for the phase velocity $c_{p|n}$ as the ratio l/λ_n (right).

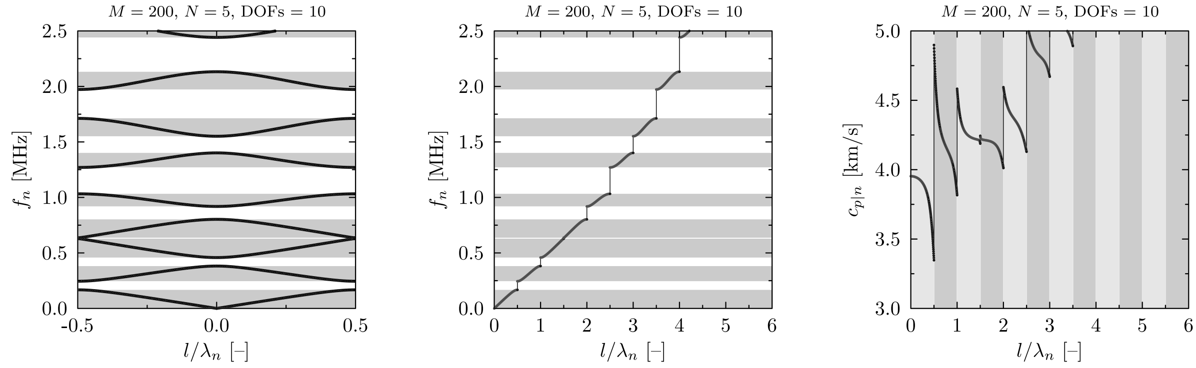

Fig. 9. Natural frequencies f_n of longitudinal modes of natural vibrations of a 1-D periodic bar of step changes in the elastic modulus, consisting $M = 200$ cells, as a function of the ratio l/λ_n: in the reduced zone (left), in the extended zone (middle), with frequency band gaps indicated in white. Numerical results obtained by the use Bloch reduction [29] and FEM, according to the classical rod theory, for a unit cell modelled by 5 rod FEs and approximation polynomials of degree $p = 2$. A resulting dispersion curve for the phase velocity $c_{p|n}$ as a function of the ratio l/λ_n (right).

(elastic modulus reduced 4 times). The results of analytical calculations obtained by the application of the Bloch theorem are presented in Fig. 7. Corresponding results of numerical calculations obtained by the application of spFEM and FEM are presented in Fig. 8 and Fig. 9. In these two cases $N = 5$ rod spFEs or FEs were used, defined according to the classical rod theory [28], for the degree of approximation polynomials $p = 2$. The total number of DOFs of the resulting FE discrete numerical models was constant and equal to 10 for both approaches.

It can be clearly seen from Fig. 7 that periodic properties of the bar (discontinuity of elastic modulus within a cell) manifest themselves as the presence of frequency band gaps in the spectrum of natural frequencies f_n. The symbols $c_{p|n}$ and λ_n in this and the following figures denote the phase velocity and the wavelength associated with the n-th mode of natural vibrations, since $c_{p|n} = f_n \lambda_n$ with $n = 1, \ldots, \text{DOFs}$. Their widths are closely correlated with the intensity of periodicity, which in the current case is dependent on the ratio $c_{p|1}/c_{p|2}$ as well as l_1/l_2. Additionally, the number of the frequency band gaps is directly dependent on the number of cells M. It is evident that discontinuities in the spectrum of natural frequencies must result in observable discontinuities in the resulting dispersion curve for the phase velocity $c_{p|n}$ (right), which are clearly indicated by phase velocity jumps. They correspond to the forbidden frequency bands, in which elastic waves cannot propagate

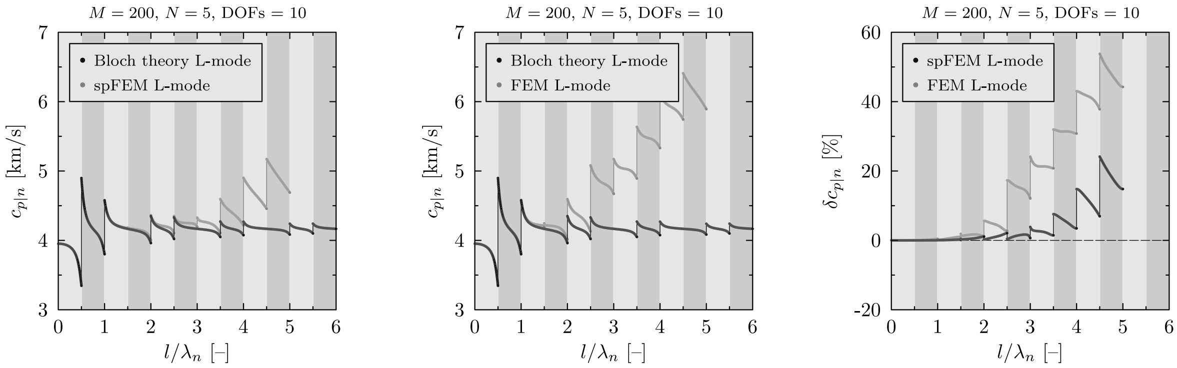

Fig. 10. Dispersion curves for the phase velocity $c_{p|n}$ of longitudinal modes of natural vibrations of a 1-D periodic bar consisting $M = 200$ cells, as a function of the ratio l/λ_n. Numerical results obtained by the use of Bloch reduction [29] and spFEM (left), FEM (middle), according to the classical rod theory, for a unit cell modelled by 5 rod spFEs/FEs and approximation polynomials of degree $p = 2$. A resulting curve for the relative error of the phase velocity $\delta c_{p|n}$ as a function of the ratio l/λ_n (right).

within the bar. Moreover, the resulting dispersion curve is non-linear and thus must lead to signal dispersion, which has it source in the periodic properties of the bar, despite the non-dispersive character of the applied rod theory.

In the case of the same bar modelled numerically by the use of spFEM and FEM the observed behaviour is similar, however, a strong influence of the numerical properties of FE discrete numerical models under investigation appears in the upper part of the natural frequency spectra. In general, this influence is smaller and leads to smaller numerical errors in the case of spFEM. It can be seen from the results presented in Fig. 8 that the position and the widths of numerically predicted frequency band gaps tend to differ with an increase in natural frequencies f_n, when compared with the analytical results presented in Fig. 7. This behaviour is due to the limited number of DOFs of each FE discrete numerical model and the degree of approximation polynomials p. In the case of FEM the observed differences are bigger, as seen in Fig. 9, and have their source not only in the FE discrete numerical model used for calculations, but also in the inherent discontinuity of the stress/strain fields between adjacent FEs, typical for FEM – please refer to Table 1 and Table 2.

Moreover, it is evident from Fig. 8 and Fig. 9 that the natural frequencies f_n calculated numerically agree very well with the analytical ones up to 1 MHz. From this point on the modelling error increases. It is expected that this error must have its source in periodic properties of numerical models themselves rather than in the material properties of the bar under investigation. Here, the modelling error, understood as the relative natural frequency error ϵ_n as well as the average natural frequency error $\bar{\epsilon}_n$, are defined in the following manner:

$$\epsilon_n = \frac{f_n - \hat{f}_n}{\hat{f}_n} \times 100\%, \quad \bar{\epsilon}_n = \frac{1}{n}\sum_{i=1}^{n} \epsilon_n \quad n = 1, \dots, M \times \text{DOFs} \tag{11}$$

where f_n denotes the value of the n-th natural frequency calculated numerically by a selected computational approach (FEM, TD-SFEM or spFEM, etc.), while $\hat{f}_n$ is its value calculated analytically by the application of the Bloch theorem. It is worth to note at this point that the relative natural frequency error ϵ_n and the relative phase velocity error $\delta c_{p|n}$ are identical, since:

$$\epsilon_n = \frac{f_n - \hat{f}_n}{\hat{f}_n} \times 100\% = \frac{f_n\lambda_n - \hat{f}_n\lambda_n}{\hat{f}_n\lambda_n} \times 100\% = \frac{c_{p|n} - \hat{c}_{p|n}}{\hat{c}_{p|n}} \times 100\% = \delta c_{p|n} \tag{12}$$

where in a similar fashion as previously $c_{p|n}$ denotes the value the phase velocity associated with the n-th natural frequency calculated numerically, while $\hat{c}_{p|n}$ is its value calculated analytically. The same applies to the average phase velocity error $\delta\bar{c}_{p|n}$.

Corresponding results are presented in Fig. 10 and confirm that the relative error of the phase velocity $\delta c_{p|n}$ is significantly smaller in the case of spFEM than in the case of FEM. For spFEM this error stays well below 5% up to the value of the ratio l/λ_n smaller than 3 (for wavelengths $\lambda_n \geq l/3$), which is 60% of its total variation range. In the case of FEM this range is shorter and reaches the value of the ratio l/λ_n smaller than 2 (for wavelengths $\lambda_n \geq l/2$). For higher values of the ratio l/λ_n both numerical approaches are characterised by greater values of the relative errors of the phase velocity $\delta c_{p|n}$, with peak values of 24% for spFEM and 54% for FEM, respectively. The average error of the phase velocity $\delta\bar{c}_{p|n}$ is smaller and equal to 4.1% for spFEM and 16.4% for FEM in the whole range of the ratio l/λ_n. These values are significantly smaller when only a part of this range is considered. For example, for the value of the ratio l/λ_n smaller than 2.5 (for wavelengths $\lambda_n \geq 2l/5$) the resulting average error of the phase velocity $\delta\bar{c}_{p|n}$ is equal to 0.4% for spFEM and 1.3% for FEM. It can be said that in the current analysis concerning two equivalent FE discrete numerical models of the bar, both modelling errors in the case of FEM are much greater than its corresponding values obtained for spFEM, as it is summarised by the results presented in Table 3 concerning the average error of the phase velocity $\delta\bar{c}_{p|n}$.

Table 3
The average error of the phase velocity $\delta\bar{c}_{p|n}$ of longitudinal modes of natural vibrations of a 1-D periodic bar consisting $M = 200$ cells, as a function of the ratio l/λ_n. Numerical results by spFEM/FEM, according to the classical rod theory, obtained by the use of Bloch reduction [29] for a unit cell modelled by 5 rod spFEs/FEs and approximation polynomials of degree $p = 2$.

Ratio l/λ_n	Range of wavelengths	spFEM $\delta\bar{c}_{p\vert n}$	FEM $\delta\bar{c}_{p\vert n}$
0 to 1	$\lambda_n \geq l$	0.0%	0.1%
0 to 2	$\lambda_n \geq l/2$	0.2%	0.6%
0 to 3	$\lambda_n \geq l/3$	0.5%	3.7%
0 to 4	$\lambda_n \geq l/4$	1.4%	9.4%
0 to 5	$\lambda_n \geq l/5$	4.1%	16.4%

It should be realised that the modelling errors discussed above have a significant impact not only on calculated numerically spectra of natural frequencies, but also on corresponding modes of natural vibrations. At this place it is worth to stop for a moment and look at a particular solution to the equation of motion in the case of excitations due to initial displacements and/or initial velocities:

$$\mathbf{M}\cdot\ddot{\mathbf{q}}(t) + \mathbf{C}\cdot\dot{\mathbf{q}}(t) + \mathbf{K}\cdot\mathbf{q}(t) = 0, \quad \mathbf{q}(0) = \mathbf{q}_0, \quad \dot{\mathbf{q}}(0) = \dot{\mathbf{q}}_0 \tag{13}$$

where $\mathbf{q}(t)$ is the displacement vector, $(\dot{\bullet})$ and $(\ddot{\bullet})$ denote the first and second derivatives with respect of time t, while $\mathbf{K}$, $\mathbf{M}$ and $\mathbf{C}$ are the stiffness, inertia and damping matrices, respectively [1].

In such a case the resulting response of a structure is a sum of all modes of natural vibrations and the solution to the equation of motion (13) can be expressed in a very well-know form:

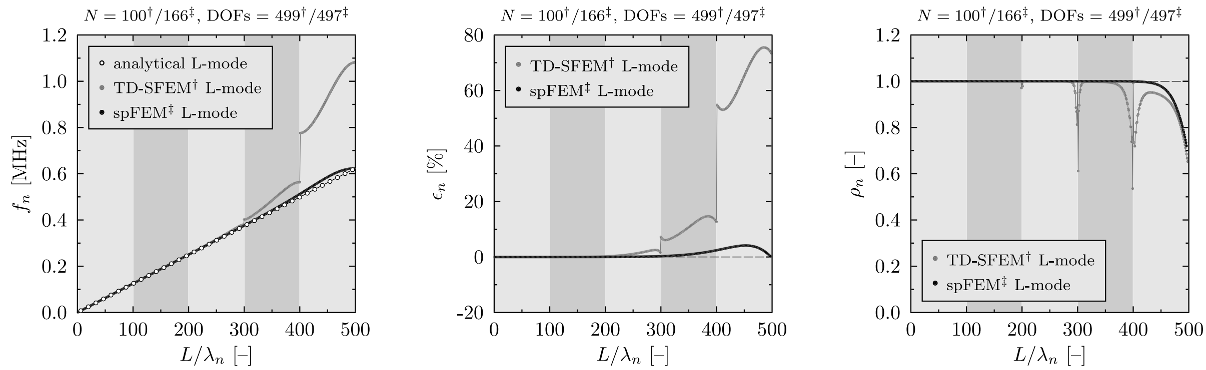

Fig. 11. Natural frequencies f_n (left), the relative natural frequency error ϵ_n (middle) and the correlation coefficient ρ_n (right) for longitudinal modes of natural vibrations of a 1-D non-periodic aluminium bar, as a function of the ratio L/λ_n. Numerical results obtained by the use of TD-SFEM and spFEM, according to the classical rod theory in the case of the bar of fixed ends, modelled by $N = 100/166$ SFEs/spFEs and approximation polynomials of degree $p = 5$ (TD-SFEM) and $p = 3$ (spFEM).

$$\mathbf{q}(t) = \sum_n \chi_n \mathbf{q}_n e^{i\omega_n t} \tag{14}$$

where χ_n is a complex amplitude of the n-th mode of natural vibrations $\mathbf{q}_n$ resulting from given initial conditions and associated with the angular natural frequency $\omega_n = 2\pi f_n$, while i is the imaginary unit. In should be emphasised that in the case of impulse excitations the sum from Eq. (14) must comprise all numerically calculated modes $\mathbf{q}_n$ and frequencies f_n of natural vibrations, therefore $n = 1, 2, \ldots,$ DOFs.

Based on the form of solution given by Eq. (14) it can be seen immediately that accurate numerical calculation of modes and frequencies of natural vibrations is a vital aspect of numerical analysis, especially in the context of wave propagation problems. For this reason numerical misrepresentation of calculated modes and frequencies of natural vibration may lead to errors, which can significantly influence or falsify calculated dynamic responses or even prevent the process of their calculation. Therefore it is very important to examine the values of modelling errors and their influence on calculated dynamic responses in the case of FE discrete numerical models, which may be considered as representing structures of properties typical to periodic structures.

4. Natural frequency spectra and wave propagation problems

4.1. Longitudinal behaviour of one-dimensional structures

4.1.1. One-mode classical rod theory

The phenomenon described in Section 3.1 is demonstrated by the results of numerical calculations presented in Fig. 11. They are related to the same bar, but having no structural periodic properties, i.e. when $c_{p|1} = c_{p|2} = c_p = 5$ km/s. Thus, the total number of cells is the bar many be assumed as identical to the number of FEs. In this case the bar of fixed ends was modelled by $N = 100/166$ rod SFEs/spFEMs (DOFs = 499/497), defined according to the classical rod theory – see *Appendix C*. In the first step the analysis carried out was related to the frequencies and modes of natural vibrations of the bar of fixed ends and for the degrees of approximation polynomials $p = 5$ and Chebyshev node distribution (TD-SFEM) and $p = 3$ (spFEM).

The results presented in Fig. 11 confirm that the FE discrete numerical model based on TD-SFEM and used in this analysis exhibits certain properties of periodic nature, in contrast to the model based on spFEM. This time it turns out that each SFE used can be assumed to represent one cell of a periodic system, so the resulting model periodicity is equal to the number of SFEs employed. As a consequence of this the calculated spectrum of natural frequencies of the bar is divided into $p = 5$ segments separated by $d = 4$ frequency band gaps, where $d = p - c - 1$, with $c = 0$ denoting the class of differentiability of approximation polynomials, as presented in Table 4.

At this place it should be noted that depending on the type of computational approach the ratio l/λ_n is directly dependent on the bar division into FEs since $l = L/N$. This is true even if the total number of DOFs of resulting FE discrete numerical models under comparison are kept the same. For this reason this ratio is replaced by a more universal measure, which is the ratio L/λ_n. This ratio not only relates the wavelength λ_l, associated with the n-th mode of natural vibration of the bar, to its total length L, but is equal to the mode number n itself. In the case of the periodic boundary conditions and the analysis extending to m zones this fact can be explained through the following simple relations:

Table 4
The influence of the type of approximation polynomials, their degree p and class of differentiability c, on the number of frequency band gaps d within the calculated natural frequency spectrum, for various types of one-mode FEM approaches.

Type of approach	Type of approx. polynomials	p	c	$d = p - c - 1$
Classical FEM	Lagrange [6,30]	1	0	0
		2	0	1
TD-SFEM	Chebyshev/Lobatto [1,30]	3	0	2
		4	0	3
		5	0	4
		⋮	⋮	⋮
Specialised FEM	Hermite [31]	3	1	1
		5	2	2
spFEM	spline [13,14]	1	0	0
		2	1	0
		3	2	0
		⋮	⋮	⋮

p – degree of approximation polynomials.
c – class of differentiability of approximation polynomials.
d – number of frequency band gaps in natural frequency spectrum.

$$k_n = \frac{2\pi}{l}\frac{n}{N} \to \frac{2\pi}{\lambda_n} = \frac{2\pi}{L}n \to \frac{L}{\lambda_n} = n, \quad n = 0, \pm 1, \pm 2 \ldots, \pm \frac{mN}{2} \tag{15}$$

It is also seen in Fig. 11 that the frequency band gaps associated with higher natural frequencies f_n, or the values of the ratio L/λ_n higher than 400 (for wavelengths $\lambda_n \leq L/400$), lead to quite significant modelling errors in the case of TD-SFEM. However, the errors from the lower part of the natural frequency spectrum can also play a significant role in the problems related to wave propagation. This is well seen in the case of the correlation coefficient ρ_n, defined below, which exhibits a small discontinuity for the value of the ratio L/λ_n equal to 200 (for wavelengths $\lambda_n = L/200$).

Based on Table 4 it can be assumed that the presence of frequency band gaps within calculated spectra of natural frequencies can be eliminated only in the case of approximation polynomials, for which their class of differentiability c is one degree smaller than their degree p, i.e. when $c = p - 1$. It is also clearly seen that this is achieved in the case of

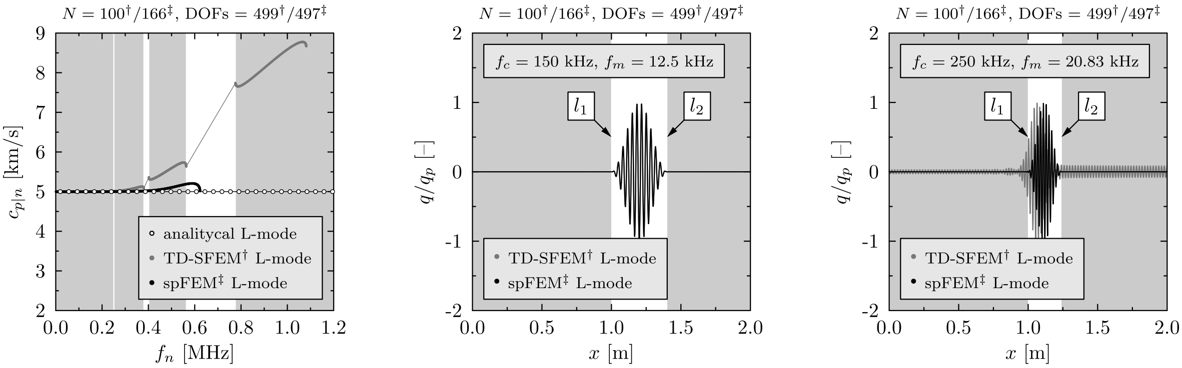

Fig. 12. Dispersion curve for the phase velocity $c_{p|n}$ for longitudinal modes of natural vibrations of a 1-D non-periodic bar, as a function of the natural frequency f_n (left), with frequency band gaps indicated in white. Non-dimensional patterns of longitudinal waves in the bar for two different carrier frequencies $f_c = 150$ kHz (middle) and $f_c = 250$ kHz (right). Numerical results obtained by the use of TD-SFEM and spFEM, according to the classical rod theory in the case of the bar of fixed ends, modelled by $N = 100/166$ SFEs/spFEs and for approximation polynomials of degree $p = 5$ (TD-SFEM) and $p = 3$ (spFEM).

FEM only for $p = 1$. However, in the case of spFEM this can be achieved for any degree of approximation polynomials p. Additionally, it should be added that the latter approach is characterised by much greater accuracy.

It can be checked that additional degrees of freedom that guarantee a higher order of differentiability of approximation polynomials, which ensures the continuity of the stress/strain fields between adjacent FEs, as in the case of Hermite approximation polynomials, is not a necessary condition to guaranty the elimination of undesired frequency band gaps and division of the calculated frequency spectra into discontinued segments.

The presence of unnoticeable frequency band gaps in the lower part of the spectrum of natural frequencies f_n of the bar under consideration has profound effects in the case of wave propagation analysis, as shown in Fig. 12. These results were obtained for the same numerical models of the bar. The dynamic responses of the bar in the time domain were calculated by the application of a higher accuracy central difference method [32]. In general, the total time of analysis T varied depending on the case. It was divided into 2^{14} time steps and chosen so that the signal propagating within the bar as elastic waves could fully reflect from the right end of the bar, reaching the bar centre. The final position of the front and end of the wave packet at the end of the analysis, calculated analytically, was denoted as l_1 and l_2, respectively.

According to the applied rod theory the phase and group velocities of elastic waves propagating in the bar are the same, i.e. $c_p = c_g = 5$ km/s, which means that no signal dispersion should be observed during the analysis. As a source of excitation a force signal $F_x(t)$ was chosen having the form of a sine wave of 12 pulses and amplitude 1 N, modulated by the Hann window. Two different carrier frequencies of the excitation were selected as $f_c = 150$ kHz as well as $f_c = 250$ kHz, with corresponding modulation frequencies $f_m = 12.5$ kHz and $f_m = 20.83$ kHz. For clarity, the results obtained are presented in Fig. 12 in a non-dimensional form, as related to their peak values q_p of the displacement response at the excitation point $x = 0$.

It is clear from Fig. 12 that the dynamic responses of the bar calculated for the carrier frequency $f_c = 150$ kHz are clear of any undesirable behaviour for both numerical approaches, which lead to the same numerical results. In contrast, the dynamic responses of the bar calculated for the carrier frequency $f_c = 250$ kHz in the case of TD-SFEM reveal some undesired behaviour manifesting in strong signal distortion as well as some dispersion. This has its origin in the periodicity of the FE discrete numerical model of the bar. However, it should also be noted that according to the results presented in Fig. 11 (middle), no significant relative natural frequency error ϵ_n in the natural frequency spectrum can be seen within this frequency range, up to the value of the ratio L/λ_n smaller than 300 (for wavelengths $\lambda_n \geq L/300$). It turns out the observed behaviour is closely related to the model inability to properly recover the modes on natural vibrations within the frequency range of interest rather than the natural frequencies, as seen in Fig. 11 (right) in the case of the correlation coefficient ρ_n.

These results explain the presence of the strong signal distortion visible, despite the fact that there are no evident frequency band gaps around the higher carrier frequency of $f_c = 250$ kHz in the spectrum of natural frequencies f_n or the dispersion curve for the phase velocity $c_{p|n}$. It is evident that in this case the correlation coefficient ρ_n has a small drop in its value just around the value of the ratio L/λ_n equal 200 (for wavelengths $\lambda \approx L/200$), which corresponds to the carrier frequency f_c. Based on [33] the authors used the correlation coefficient ρ_n defined as:

$$\rho_n(\mathbf{p}_n, \hat{\mathbf{p}}_n) = \frac{1}{N} \sum_{i=1}^{N} \left(\frac{p_{n,i} - \mu}{\sigma} \right) \left(\frac{\hat{p}_{n,i} - \hat{\mu}}{\hat{\sigma}} \right), \quad n = 1, 2, \ldots, \text{DOFs} \tag{16}$$

where $\mathbf{p}_n$ is a FFT-based power spectral density associated with the modal displacement vector $\mathbf{q}_n$ for the n-th mode of natural vibrations calculated numerically, $\hat{\mathbf{p}}_n$ associated with the modal displacement vector calculated analytically, with μ and σ being the mean value and the standard deviation of $\mathbf{p}_n$, with $\hat{\mu}$ and $\hat{\sigma}$ being the mean value and the standard deviation of $\hat{\mathbf{p}}_n$. It should be added that calculation of the correlation coefficient ρ_n was based on a number of points, evenly distributed along the bar, at least 100 times greater than total number of DOFs of FE discrete numerical models.

The observation made is well supported by the distribution of the relative error of mode representation ϵ'_n, understood as the relative error of modal displacements calculated along the bar at the same points based on the application of the Hilbert transform (signal envelope), and expressed as follows:

$$\epsilon'_n = \frac{|H(\mathbf{q}_n)| - |H(\hat{\mathbf{q}}_n)|}{|H(\hat{\mathbf{q}}_n)|} \times 100\%, \quad n = 1, \ldots, \text{DOFs} \tag{17}$$

where as before $\mathbf{q}_n$ is the modal displacement vector associated with the n-th natural frequency calculated numerically, $\hat{\mathbf{q}}_n$ is its value calculated analytically, while $H(\bullet)$ denotes the Hilbert transform.

The distribution of the relative error of mode representation ϵ'_n, presented in Fig. 13, indicates clearly that around the higher carrier frequency $f_c = 250$ kHz calculated modal responses of the bar are based on significantly distorted modes of natural vibrations in the case of TD-SFEM (middle). This is caused by the nearby frequency band gap, which is associated just with mode #200 (for the value of the ratio $L/\lambda \approx 200$ or wavelengths $\lambda \approx L/200$). In the case of the lower carrier frequency $f_c = 150$ kHz (for the value of the ratio $L/\lambda \approx 120$ or wavelengths $\lambda \approx L/120$) kHz, this problem in not seen.

The behaviour described above fully supports the statement that the usable part of the frequency spectrum of the bar under consideration, which guarantees high accuracy of computational results in the case of TD-SFEM, ends just before the values of the ratio L/λ_n equal to 200 (for

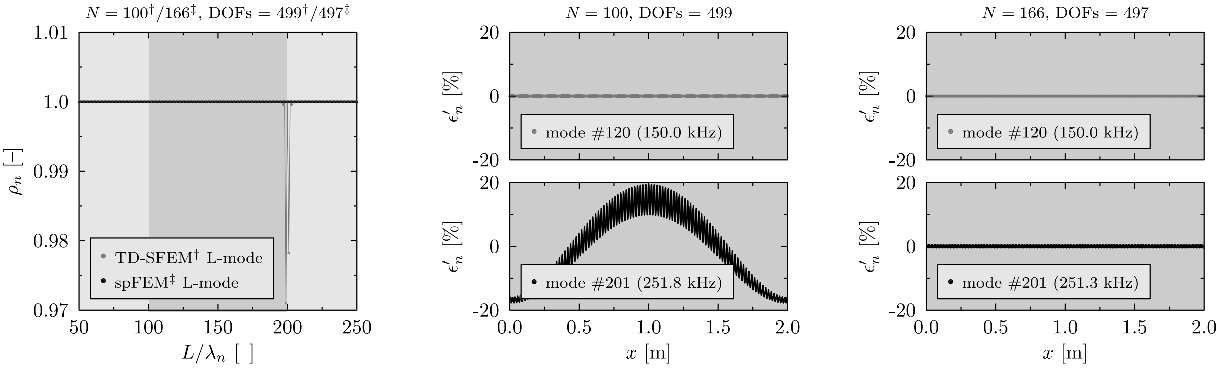

Fig. 13. Correlation coefficient ρ_n for longitudinal modes of natural vibrations of a 1-D non-periodic bar, as a function of the ratio l/λ_n (left). Distributions of the relative error of mode representation ϵ'_n along the bar. Numerical results obtained by the use of TD-SFEM (middle) and spFEM (right), according to the classical rod theory in the case of the bar of fixed ends, modelled by $N = 100/166$ SFEs/spFEs and for approximation polynomials of degree $p = 5$ (TD-SFEM) and $p = 3$ (spFEM).

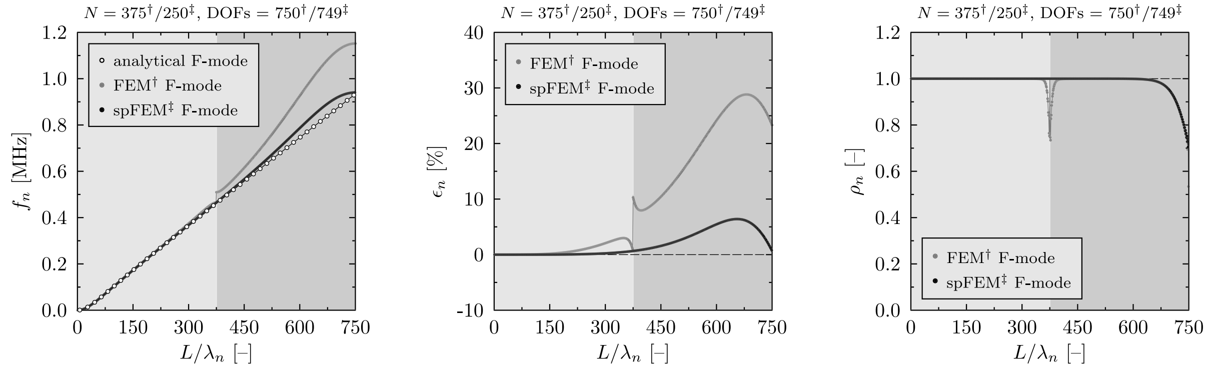

Fig. 14. Natural frequencies f_n (left), the relative natural frequency error ϵ_n (middle) and the correlation coefficient ρ_n (right) of flexural modes of natural vibrations of a 1-D non-periodic aluminium bar, as a function of the ratio L/λ_n. Numerical results obtained by the use of FEM and spFEM, according to the classical beam theory in the case of the bar of simply-supported ends, modelled by $N = 375/250$ FEs/spFEs and for approximation polynomials of degree $p = 3$ (FEM) and $p = 3$ (spFEM).

wavelengths $\lambda_n \geq L/200$). This comprises the first 200 frequencies and modes of natural vibrations, which effectively reduces this spectrum to 40% of its total span. It can be mentioned that then the correlation coefficient ρ_n drops down to 97%. Despite the fact that this drop seems relatively small, it has a significant impact on calculated dynamical responses in the case of the excitation frequencies from the vicinity of the frequencies associated with the ratio L/λ_n approximately equal to 200 (for wavelengths $\lambda \approx L/200$).

However, in the case of the bar modelled by spFEM and the use of the spline-based elemental shape functions, this problem is not observed. The continuity of the shape functions and their first and second derivatives leads to a smooth spectrum of natural frequencies of the bar, which is free of any frequency band gaps – in this case $d = p - c - 1 = 0$. It is not only that the spectrum of natural frequencies calculated by the use of spFEM is smooth, but calculated natural frequencies of the bar are characterised by small values of the relative natural frequency error ϵ_n, which reaches only 4.13%, as it can be seen from Fig. 11 (left). This value is very low in comparison to the corresponding results obtained for TD-SFEM, were the maximum value of this error ϵ_n reaches 75.5%.

It is also visible from Fig. 12 that the dynamic responses of the bar, calculated for the same carrier frequencies f_c = 150 kHz and f_c = 250 kHz, are clear of any undesirable behaviour in the case of spFEM. The behaviour observed has this time its source in the ability of the FE discrete numerical model to properly recover the modes of natural vibrations within the frequency range of interest, as seen in Fig. 11 (right). Moreover, in the case of spFEM this range extends nearly to the entire spectrum of natural frequencies f_n and is limited only by a drop in the correlation coefficient ρ_n at the end of this spectrum. For practical purposes it can be assumed that the value of the correlation coefficient ρ_n should not be smaller than 97%. In the case of spFEM such an assumption effectively reduces the usable part of the natural frequency spectrum to 78.5% of its total span.

4.2. *Flexural behaviour of one-dimensional structures*

4.2.1. *One-mode Bernoulli-Euler beam theory*

Taking into account the result presented and discussed previously, the authors decided to focus their attention on two similar types of FEs approaches. In the first case the classical FEM approach was used, for which Hermite approximation polynomials of degree $p = 3$ were employed. In the second case spFEM was used and spline-based approximation polynomials of the same degree $p = 3$ were employed, which provide not only the continuity of the unknown displacement functions and their first derivatives, but also their second derivatives.

The results shown in Fig. 14 are related to the flexural behaviour of the aluminium bar under investigation, modelled according to the classical beam theory [30] – see *Appendix D*. Both computational approaches are considered, i.e. FEM and spFEM. In this case the bar of simply-supported ends was modelled by $N = 375/250$ classical beam FEs/spFEMs (DOFs = 750/749). It should be noted here that in the current case as a source of excitation a transverse force signal $F_y(t)$ was chosen, as presented in Fig. 6, having the same form as before. Additionally, it is known that in the specialised FEM approach, thanks to the use of the approximation polynomials in the form of Hermite polynomials of degree $p = 3$, the continuity of the unknown displacement functions and their first derivatives is provided, i.e. the stress/strain fields between adjacent FEs remains continuous, in a similar manner as in the case of spFEM.

As in the case of the longitudinal behaviour of the bar discussed in Section 4.1, the results presented in Fig. 14 confirm that the FE discrete

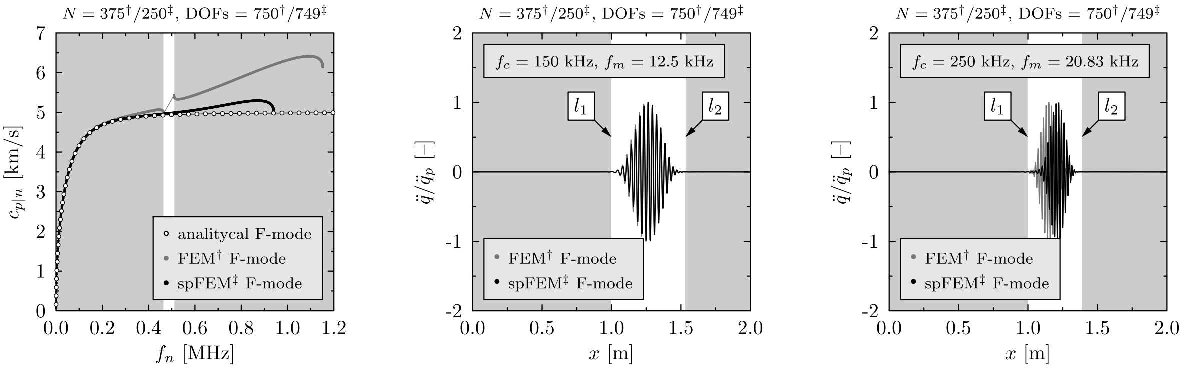

Fig. 15. A dispersion curve for the phase velocity $c_{p|n}$ of flexural modes of natural vibrations of a 1-D non-periodic bar, as a function of the natural frequency f_n (left), with a frequency band gap indicated in white. Non-dimensional patterns of flexural waves in the bar for two different carrier frequencies $f_c = 150$ kHz (middle) and $f_c = 250$ kHz (right). Numerical results obtained by the use of FEM and spFEM, according to the classical beam in the case of the bar of simply-supported ends, modelled by $N = 375/250$ FEs/spFEs and for approximation polynomials of degree $p = 3$ (FEM) and $p = 3$ (spFEM).

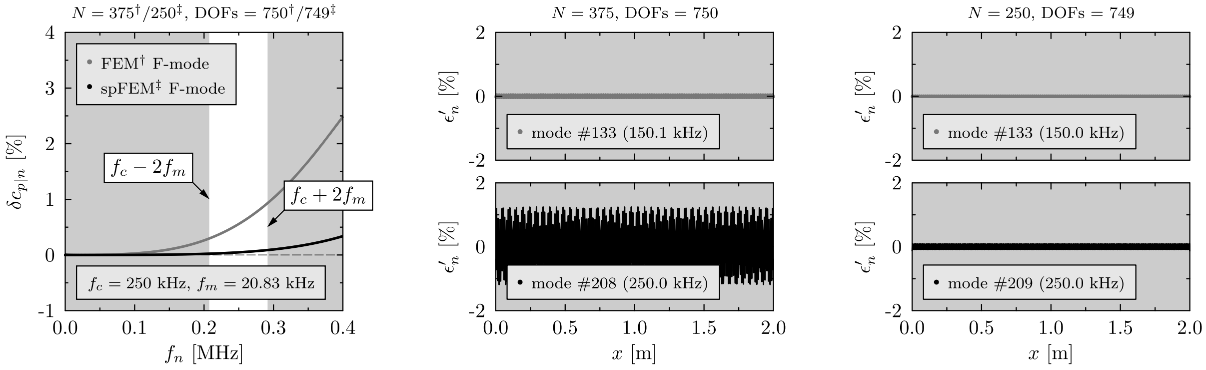

Fig. 16. The relative error of the phase velocity $\delta c_{p|n}$ of flexural modes of natural vibrations of a 1-D non-periodic bar, as a function of the natural frequency f_n (left). Distributions of the relative error of mode representation ϵ'_n along the bar. Numerical results obtained by the use of FEM, according to the classical beam theory in the case of the bar of simply-supported ends, modelled by $N = 375/250$ FEs/spFEs and for approximation polynomials of degree $p = 3$ (FEM) and $p = 3$ (spFEM).

numerical model used for FEM in this analysis also exhibits properties of periodic nature. As before the resulting model periodicity is correlated to the number of FEs employed. As a consequence of this, according to Table 4, the calculated spectrum of natural frequencies of the bar must be divided into $p = 2$ segments separated by $d = 1$ frequency band gaps, where $d = p - c - 1$ with $c = 1$ being the class of differentiability of approximation polynomials. It is also seen that the presence of the frequency band gap can have a significant influence on numerical errors associated with higher natural frequencies f_n, however, the errors from the lower part of the natural frequency spectrum again can play a significant role in the problems related to wave propagation.

According to the applied beam theory the phase and group velocities of elastic waves propagating in the bar are different, i.e. $c_p \neq c_g$, which means that some signal dispersion should be observed during the analysis. As a source of excitation the same force signal $F_x(t)$ was chosen and the same values of carrier frequencies of the excitation were selected as $f_c = 150$ kHz as well as $f_c = 250$ kHz, with corresponding modulation frequencies $f_m = 12.5$ kHz and $f_m = 20.83$ kHz. For clarity, the results obtained are presented in Fig. 15 in a non-dimensional form, as related to their peak value $\ddot{q}_p$ of the acceleration response at the excitation point $x = 0$.

It is clear from Fig. 15 (middle) that the dynamic responses of the bar calculated for the carrier frequency $f_c = 150$ kHz (left) are clear of any undesirable behaviour. However, the dynamic responses of the bar calculated for the carrier frequency $f_c = 250$ kHz (right) reveal some undesired behaviour manifesting in an increased propagation speed, slight signal distortion as well as some dispersion, which again has its origin in the periodicity of the FE numerical model itself. However, it should also be noted that according to the results presented in Fig. 14 (middle), only small errors in the spectrum of natural frequencies f_n can be seen for the values of the ratio L/λ_n smaller than 375 (for wavelengths $\lambda \geq L/375$). It turns out this time that the observed behaviour is closely related not to the model inability to properly recover the modes on natural vibrations within the frequency range of interest, but primarily to the relative error of the phase velocity $\delta c_{p|n}$, which increases up to 3% towards the frequency band gap near the value of the ratio L/λ_n equal 375, as seen in Fig. 14 (middle).

This is also confirmed by the results presented in Fig. 16, which concern the relative error of the phase velocity $\delta c_{p|n}$ and the distribution of relative errors of mode representation ϵ'_n. It can be seen that their values near the carrier frequency $f_c = 150$ kHz and $f_c = 250$ kHz are very small and as such should not be considered as responsible for the observed behaviour.

Based on the results presented in Fig. 16 (left) it can be concluded that within the range of natural frequencies f_n up to the carrier frequency $f_c = 250$ kHz the relative error of the phase velocity $\delta c_{p|n}$ remains small, not exceeding 0.6%. However, this is not the case for the error related to the group velocity $c_{g|n}$, corresponding to the n-th mode of natural vibration, which can be calculated from a simple relation [34]:

$$c_{g|n} = \frac{d\omega_n}{dk_n}, \quad c_{p|n} = \frac{\omega_n}{k_n}, \quad c_{g|n} = \frac{d(k_n c_{p|n})}{dk_n} = c_{p|n} + k_n \frac{dc_{p|n}}{dk_n}, \quad n = 1, \dots, \text{DOFs} \tag{18}$$

It can be immediately seen from Eq. (18) that the relative error of the group velocity $\delta c_{g|n}$, associated with the n-th mode of natural vibrations, increases with wave numbers k_n and can be much greater than the corresponding relative error of the phase velocity $\delta c_{p|n}$, as long as

Table 5
The relative errors of the phase $\delta c_{p|n}$ and group $\delta c_{g|n}$ velocities as a function of the coefficient k together with signal energy content E, calculated in the case of the signal carrier frequency $f_c = 150$ kHz and modulation frequency $f_c = 12.5$ kHz. Numerical results obtained by the use of FEM, according to the classical beam theory in the case of the bar of simply-supported ends, modelled by $N = 375$ FEs and for approximation polynomials of degree $p = 3$.

k [–]	$f_c - kf_m \approx f_{n_1}$ [kHz]	$f_c + kf_m \approx f_{n_2}$ [kHz]	n_1 [–]	n_2 [–]	$\delta c_{p\|n_1}$ [%]	$\delta c_{p\|n_2}$ [%]	$\delta c_{g\|n_1}$ [%]	$\delta c_{g\|n_2}$ [%]	E [%]
1	137.5	162.5	124	142	0.08	0.13	0.33	0.57	79.1
2	125.0	175.0	114	152	0.05	0.17	0.23	0.75	97.3
3	112.5	187.5	105	161	0.04	0.21	0.17	0.94	98.9
4	100.0	200.0	96	171	0.03	0.27	0.12	1.18	99.4
5	87.5	212.5	87	180	0.02	0.32	0.08	1.44	99.6

Table 6
The relative errors of the phase $\delta c_{p|n}$ and group $\delta c_{g|n}$ velocities as a function of the coefficient k together with signal energy content E, calculated in the case of the signal carrier frequency $f_c = 250$ kHz and modulation frequency $f_c = 20.8$ kHz. Numerical results obtained by the use of FEM, according to the classical beam theory in the case of the bar of simply-supported ends, modelled by $N = 375$ FEs and for approximation polynomials of degree $p = 3$.

k [–]	$f_c - kf_m \approx f_{n_1}$ [kHz]	$f_c + kf_m \approx f_{n_2}$ [kHz]	n_1 [–]	n_2 [–]	$\delta c_{p\|n_1}$ [%]	$\delta c_{p\|n_2}$ [%]	$\delta c_{g\|n_1}$ [%]	$\delta c_{g\|n_2}$ [%]	E [%]
1	229.2	270.8	192	225	0.41	0.75	1.85	3.32	77.6
2	208.3	291.7	177	241	0.30	0.96	1.35	4.26	97.3
3	187.5	312.5	161	258	0.21	1.23	0.94	5.41	98.9
4	166.7	333.3	146	275	0.15	1.52	0.64	6.60	99.4
5	145.8	354.2	130	290	0.09	1.84	0.40	7.83	99.6

$dc_{p|n}/dk_n > 0$. This condition is fulfilled in the case of the results presented in Fig. 16, what is summarised in Table 5 and Table 6.

Despite the fact that the majority of the excitation signal energy falls into a relatively narrow window of frequencies $f_c \pm 2f_m$, as shown in [1], the spectrum of excited frequencies is in fact broader and can be assumed to cover a wider frequency range. In the context of the results presented in Table 5 and Table 6 it becomes obvious that the entire energy E of the propagating signal must extend onto a wider window of frequencies. In the case of the factor $k = 2$ the signal energy E with the range of frequencies $f_c \pm 2f_m$ reaches 97.3%, while in the case of the factor $k = 5$ the signal energy E within the range of frequencies $f_c \pm 5f_m$ reaches 99.6%. It turns out that the modelling error expressed in terms of the relative error of the group velocity $\delta c_{g|n}$, in an increased window of frequencies, helps to explain the behaviour of the propagating flexural waves in the bar.

The results presented in Table 6 show that the relative error of the group velocity $\delta c_{g|n}$ is more than four times greater than the relative error of the phase velocity $\delta c_{p|n}$. It increases up to 4.26% for the factor $k = 2$, while it reaches 7.83% for the factor $k = 5$. Bearing in mind that the group velocity c_g exceeds 5 km/s in the case of all values of the factor k, the relative error of the group velocity $\delta c_{g|n} = 5\%$. This corresponds to the distance of 0.15 m, which is nearly 40% of the total length of the propagating wave packet, expressed in terms of the final position of the front and end of the wave packet at the end of the analysis, calculated analytically and denoted as l_1 and l_2. This observation well corresponds to the results presented in Fig. 15.

In a similar manner as in the case of the longitudinal behaviour of the bar, the behaviour described above fully supports the statement that the usable part of the frequency spectrum of the bar under consideration, which guarantees high accuracy of computational results, ends just before the first frequency band gap. This comprises the first 365 frequencies and modes of natural vibrations, which effectively reduces the usable part of the calculated spectrum to 48.7% of its total span.

As before, also in the case of the analysis of flexural behaviour of the aluminium bar under investigation modelled by spFEs, the problems arising from the periodic nature of the FE discrete numerical model, resulting from the discontinuity of the shape functions, are not present. The continuity of the spline-based elemental shape functions and their first and second derivatives leads to a smooth spectrum of natural frequencies f_n, which is free of any frequency band gaps, since in this case $d = p - c - 1 = 0$. This is well illustrated by the results presented in Fig. 14 (left). It is not only that the spectrum of natural frequencies calculated by the use of 250 spFEs is smooth, but calculated natural frequencies of the bar are characterised by small values of the relative natural frequency error ϵ_n, which reaches 6.40% for the ratio $L/\lambda_n \approx 650$, as it can be seen from Fig. 14 (middle). This value is very low in comparison to the corresponding results obtained for FEM, were the maximum value of this error reaches 28.8% in the same region.

It is also visible from Fig. 16 (right) that the dynamic responses of the bar, calculated for the same carrier frequencies $f_c = 150$ kHz and $f_c = 250$ kHz, are clear of any undesirable behaviour. Again, this is contrary to the case of the bar modelled by FEM. The behaviour observed has the same source in the ability of the FE discrete numerical model to properly recover the modes on natural vibrations within the frequency range of interest, as seen in Fig. 14 (right). Moreover, this range extends nearly to the entire frequency spectrum and is limited only by a drop in the correlation coefficient ρ_n near the end of the spectrum. For practical purposes it can be assumed that the value of the correlation coefficient ρ_n should not be smaller than 97%, which value corresponds to the ratio L/λ_n equal to 686. This effectively reduces the usable spectrum to 91.5% of its total span.

4.2.2. *Two-mode Timoshenko beam theory*

It is interesting to see how the periodic properties of a FE discrete numerical model influence calculated dynamic characteristics in the case of a multi-mode theory. The results presented in this paragraph are related to the analysis of dynamic characteristics and propagation of elastic waves in the same bar, but when a two-mode Timoshenko beam theory is applied – see *Appendix E*. The application of TD-SFEM and spFEM are investigated in the case of the bar of simply-supported ends modelled by N = 100/166 SFEs/spFEM (DOFS = 1000/966). The FEs employed in the current computations were defined according to the Timoshenko beam theory [30], for the degree of approximation polynomials $p = 5$ and Chebyshev node distribution (TD-SFEM) as well as $p = 3$ (spFEM).

In a similar manner as in the case of previously discussed one-mode theories, it is expected now that for TD-SFEM the calculated spectrum of natural frequencies f_n of the bar should be divided into $p = 5$ seg-

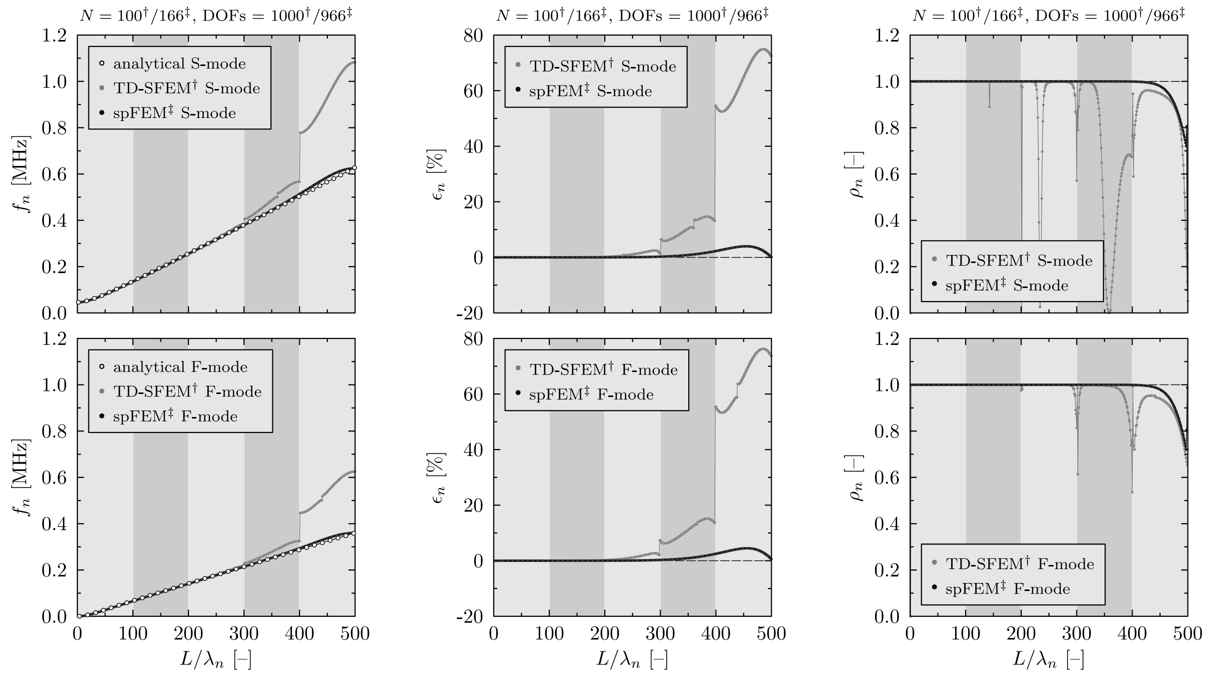

Fig. 17. Natural frequencies f_n (left), the relative natural frequency error ϵ_n (middle) and the correlation coefficient ρ_n (right) of flexural modes of natural vibrations of a 1-D non-periodic aluminium bar, as a function of the ratio L/λ_n. Numerical results obtained by the use of TD-SFEM and spFEM, according to the Timoshenko beam theory in the case of the bar of simply-supported ends, modelled by $N = 100/66$ SFEs/spFEs and for approximation polynomials of degree $p = 5$ (TD-FEM) and $p = 3$ (spFEM).

ments separated by a number of frequency band gaps, which is directly correlated with the degree of approximation polynomials p and their class of differentiability c, as presented in Table 4. However, due to the two-mode nature of the applied beam theory this should be applicable independently to each of the modes available, i.e. the flexural F-mode and the shear S-mode. As a result of this the number of frequency band gaps d, in the calculated spectrum of natural frequencies of the bar, can be doubled. What is more, a couple interaction of the two modes may result in the appearance of new frequency band gaps. Also in this case for numerical computation as a source of excitation a pure transverse force signal $F_y(t)$ was chosen, as presented in Fig. 6, having the same form as before.

The appearance of new frequency band gaps in the spectrum of natural frequencies of the bar is well illustrated by the results of numerical calculations presented in Fig. 17, which concern both modelling approaches. It can be clearly seen from Fig. 17 that in the case of TD-SFEM the spectrum of natural frequencies f_n of the bar can be viewed as divided into $p = 5$ segments, but the total number of frequency band gaps present in the spectrum is more than 10. However, the frequency band gaps associated with the natural frequencies f_n near 510 kHz (0.51 MHz) form a common frequency band gap for both modes (for the ratio L/λ_n equal 440 in the case of the flexural F-mode and L/λ_n equal 360 in the case of the shear S-mode), while the remaining frequency band gaps are independent. In comparison to that the spectrum of natural frequencies f_n of the bar, calculated based on the use of spFEM remains smooth for both modes and no frequency band gaps are present there.

As before the observed behaviour has a direct impact on the accuracy of the FE discrete numerical models, which again can be expressed in terms of the relative natural frequency error ϵ_n. It is shown in Fig. 17 (middle) that for TD-SFEM the relative natural frequency error ϵ_n slowly increases with the ratio L/λ_n and remains small for its values smaller than 300 (for wavelengths $\lambda_n \geq L/300$). It reaches its local maximum values of 2.70% for the flexural F-mode, and 2.47% for the shear S-mode, for the value of the ratio $L/\lambda_n = 290$ (for wavelengths $\lambda_n = L/290$). However, the maximum value of the relative natural frequency error ϵ_n reaches 76.3% for the F-mode and 74.9% for S-mode, for the value of the ratio $L/\lambda_n = 485$ (for wavelengths $\lambda_n = L/485$). Bearing in mind the results obtained in the case of one-mode classical rod theory, presented in Fig. 13 and Fig. 16, it can be expected that in the current case the presence of the frequency bad gaps in the lower part of the calculated spectrum may have a significant impact on both modes during the analysis of wave propagation.

Indeed, the results presented in Fig. 18 confirm this. Additionally, it should be pointed out here that because of the multi-mode nature of the problem both modes propagating in the bar, i.e. flexural and shear modes, can interact with one another, what leads to mode conversion [34,35]. Moreover, due to a non-linear dependence of the frequency f_n from the wave number k_n, which is directly dependent on the mode number n according to Eq. (15), some dispersion of propagating signals should be observed.

The presence of frequency band gaps results in a significant distortion of the calculated dynamic response yet in the case of the lower value of the carrier frequency $f_c = 150$ kHz. In this particular case the total time of analysis T was calculated based on the speed of the flexural F-mode. It is evident that in this lower frequency regime the FE discrete numerical model of the bar based on the TD-SFEM was unable to properly recreate not only the natural frequencies, but also associated modes of natural vibrations, based on which the presented responses were calculated. As a result of this the speed of both propagating modes in the bar are slightly increased in the comparison to the analytically calculated values, which can be clearly observed in Fig. 18 (middle). Also associated modes of natural vibrations are distorted, which manifests in a constant, not vanishing, level of vibrations in the beam present in front and behind the propagating wave packet. The observed behaviour significantly worsens for the higher value of the carrier frequency $f_c = 250$ kHz, as presented in Fig. 18 (right). In this case the total time of analysis T was calculated based on the speed of the shear S-mode.

Since a part of the frequency content of the excitation signal falls into frequency band gaps associated with both modes (two significant frequency band gaps for the flexural F-mode and two significant frequency band gaps for the shear S-mode) in the range of natural fre-

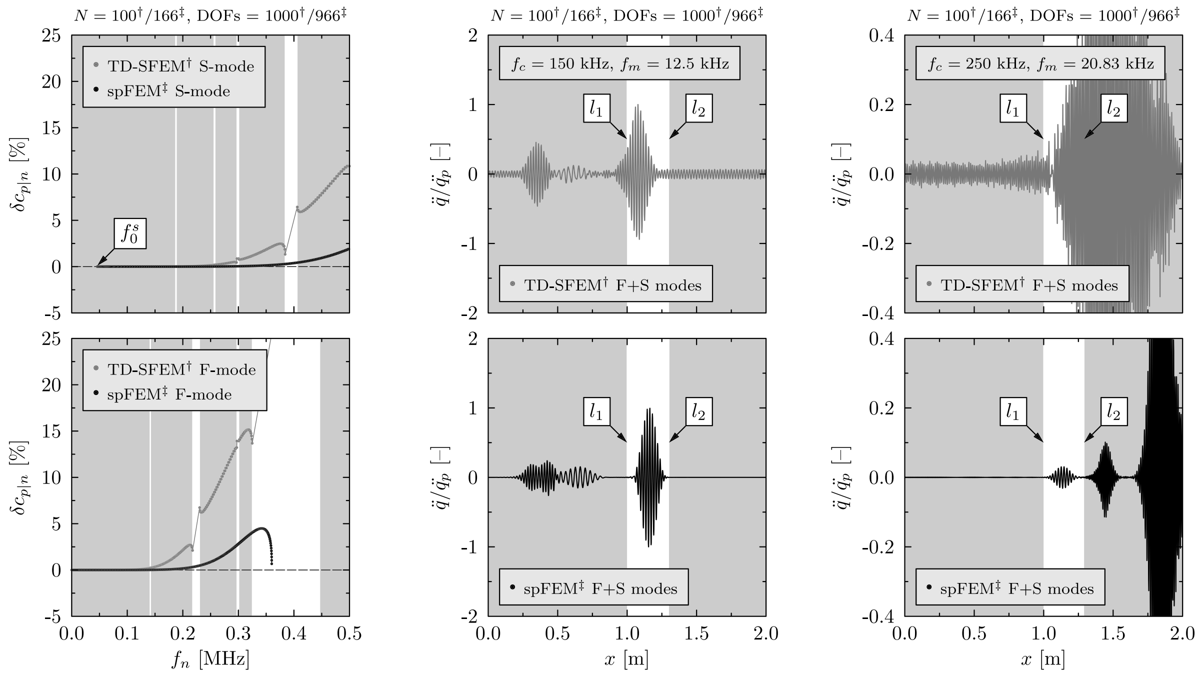

Fig. 18. The relative error of the phase velocity $\delta c_{p|n}$ of flexural modes of natural vibrations of a 1-D non-periodic aluminium bar, as a function of the natural frequency f_n (left), with frequency band gaps indicated in white. Non-dimensional patterns of flexural waves in the bar for two different carrier frequencies $f_c = 150$ kHz (middle) and $f_c = 250$ kHz (right). Numerical results obtained by the use of TD-SFEM and spFEM, according to the Timoshenko beam theory in the case of the bar of simply-supported ends, modelled by $N = 100/166$ SFEs/spFEs and approximation polynomials of degree $p = 5$ (TD-SFEM) and $p = 3$ (spFEM).

quencies f_n up to 300 kHz, the associated modes of natural vibrations must be greatly distorted. As a consequence the obtained wave propagation patterns, based on the modes of natural vibrations in the range of excited frequencies, as presented in Table 6, must be polluted by the presence of waves trapped in the bar. These trapped waves are associated with the range of natural frequencies f_n directly corresponding to all frequency band gaps within the range of frequencies excited by the excitation signal.

In contrast, the behaviour related to the use of TD-SFEM is not observable for spFEM in the case of both carrier frequencies $f_c = 150$ kHz and $f_c = 250$ kHz of the excitation. It can be seen from Fig. 18 (left) that the relative error of the phase velocity $\delta c_{p|n}$ slowly increases for spFEM, which should manifest in a slightly increased wave propagation speed in the case of the flexural F-mode. It should be noted that the value of this error is relatively small and reaches at its maximum 4.5%. However, based on the result discussed in Section 4.2.1 concerning one-mode Bernoulli-Euler beam theory, as well as the results presented in Table 6, this value of the error may have a strong influence on an increased value in the wave propagation speed of the flexural F-mode. It is interesting to see that the highest natural frequency associated with this mode, for the current FE discrete numerical model, ends up at 360 kHz, which according to Table 6 suffice to support the flexural F-mode for the higher carrier frequency $f_c = 250$ kHz of the excitation. It is also clearly seen from the results presented in Fig. 18 that in the case of spFEM the smooth spectrum of the natural frequencies f_n leads to unpolluted and clear wave propagation patterns, where the final positions of the front and end of the propagating wave packets associated with both modes fully agree with the values calculated analytically and denoted as l_1 and l_2.

5. Additional features of spFEM

In this section certain additional features of the current spFEM formulation are discussed by the authors. One of the biggest advantages of the presented approach, based on the use of piecewise 1-D spline-based elemental shape functions, is the ability to modify the nodal compatibility conditions, presented in Section 2 and expressed by Eq. (2), for selected internal nodes x_i.

Depending on the degree of approximation polynomials p, these conditions may be successfully utilised to adopt elemental shape functions of a spFEM to some specific cases, such as:

- Modelling of a step change in the cross-section and/or elastic modulus of the bar:
  - for longitudinal behaviour:

$$f_1'(x_i) = f_2'(x_i) \rightarrow ESf_1'(x_i) = (E + \Delta E)(S + \Delta S)f_2'(x_i) \tag{19}$$

  - for flexural behaviour:

$$f_1''(x_i) = f_2''(x_i) \rightarrow EIf_1'(x_i) = (E + \Delta E)(I + \Delta I)f_2'(x_i) \tag{20}$$

  where S and I are the area and the second moment of area of the bar cross-section, while E is the elastic modulus of the bar material. Appropriate step changes in their values are denoted as: ΔS, ΔI and ΔE, respectively. It should be noted that Eq. (19) and Eq. (19) result from the continuity of axial forces (longitudinal behaviour) or bending moments (flexural behaviour) between appropriate sections of the spFE.
- Modelling of internal damage in the form of a fatigue crack:
  - for longitudinal behaviour:

$$f_1(x_i) = f_2(x_i) \rightarrow f_1(x_i) - f_2(x_i) = c_{11}ESf_1'(x_i) \tag{21}$$

  - for flexural behaviour:

$$f_1'(x_i) = f_2'(x_i) \rightarrow f_1'(x_i) - f_2'(x_i) = c_{55}EIf_1''(x_i) \tag{22}$$

  where additional compliance $c_{11} = \tilde{c}_{11}R$ and $c_{55} = \tilde{c}_{55}R$, with R being the bar radius, represent the loss of bar stiffness due to the presence of a fatigue crack. The values of c_{11} and c_{55} can be easily calculated according to the laws of fracture mechanics, as presented in [36–38].

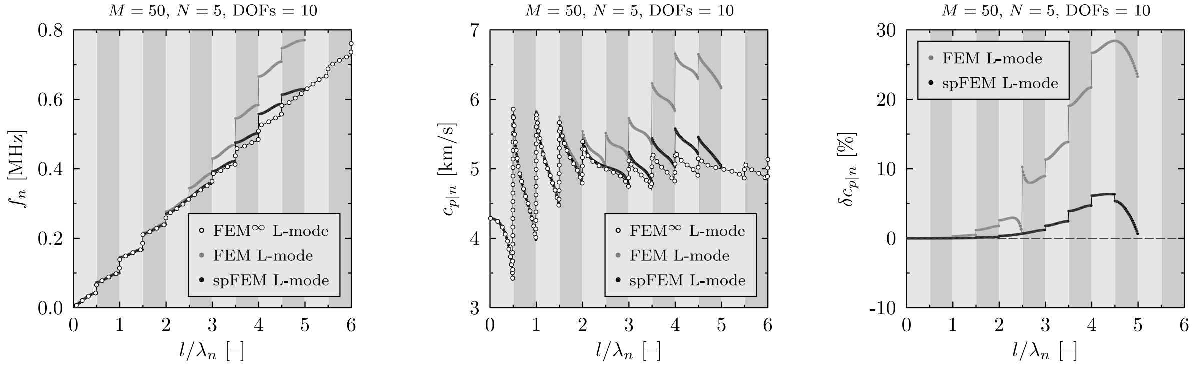

Fig. 19. Natural frequencies f_n (left), the dispersion curve for the phase velocity $c_{p|n}$ (middle), the relative error of the phase velocity $\delta c_{p|n}$ (right), of longitudinal modes of natural vibrations of a 1-D periodic bar of step changes in the cross-section, consisting $M = 50$ cells, as a function of the ratio l/λ_n. Numerical results obtained by the use of Bloch reduction [29] for FEM and spFEM, according to the classical rod theory, for a unit cell modelled by 5 rod FEs/spFEs and approximation polynomials of degree $p = 2$.

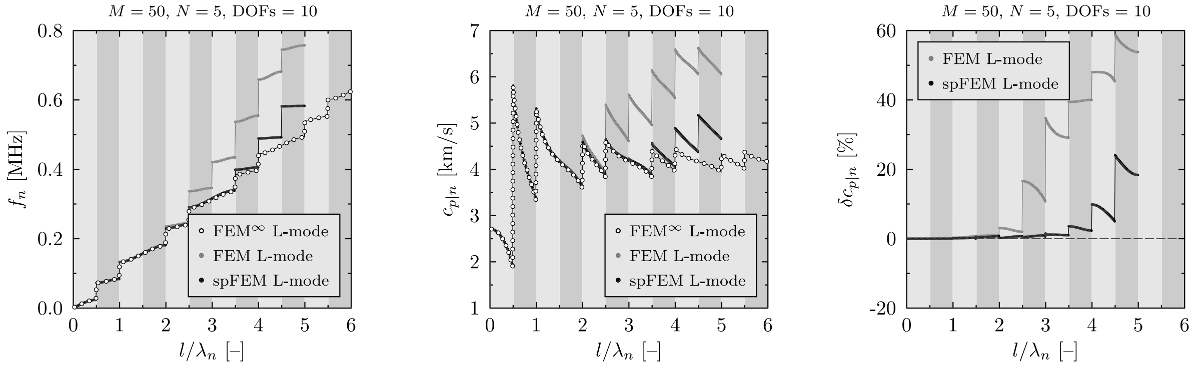

Fig. 20. Natural frequencies f_n (left), the dispersion curve for the phase velocity $c_{p|n}$ (middle), the relative error of the phase velocity $\delta c_{p|n}$ (right), of longitudinal modes of natural vibrations of a 1-D periodic bar of step changes in the cross-section and elastic modulus, consisting $M = 50$ cells, as a function of the ratio l/λ_n. Numerical results obtained by the use of Bloch reduction [29] and FEM and spFEM, according to the classical rod theory, for a unit cell modelled by 5 rod FEs/spFEs and approximation polynomials of degree $p = 2$.

- Modelling of a pin joint. A pin joint can be effectively modelled in a straightforward manner thanks to separation of appropriate rotational DOFs and their spatial derivatives, within the spFE forming a pin joint. This separation should take place during the assembling process of the characteristic stiffness **K** and inertia **M** matrices, when connectivity between particular DOFs of adjacent spFEs is determined. It can be noted that the behaviour of a pin joint can be approximated in the case of a fatigue crack described by Eq. (22), when the total area of the crack reaches the total area of the beam cross-section. This corresponds to the total loss of stiffness linking selected rotational DOFs within the spFEM, which model a pin joint.

The modelling methods discussed above, which allow one to employ the additional features of the current spFEM approach, are illustrated below. In the first case natural frequencies f_n and dispersion curves of the phase velocity $c_{p|n}$ of a 1-D periodic bar of step changes in the cross-section are investigated. The results of numerical simulation, shown in Fig. 19, concern the case of the bar consisting of $M = 50$ cells. The source of the periodicity in each cell comes from the reduction in the bar cross-section to 25% of its original value, over the distance equal to 20% of the cell length. The Bloch reduction [29] was used for FEM and spFEM discrete numerical models, built according to the classical rod theory, for a unit cell modelled by $N = 5$ classical rod FEs/spFEs (DOFs = 10) and approximation polynomials of degree $p = 2$.

It is clearly seen from Fig. 19 that the application of spFEM leads to much smaller relative errors of the phase velocity $\delta c_{p|n}$ than the application of FEM. This is true for the entire spectrum of calculated frequencies f_n as well as the entire range of the ratio l/λ_n. A part of this spectrum, characterised by the relative error of the phase velocity $\delta c_{p|n}$ (right) smaller than 5%, comprises as much as 80% of calculated natural frequencies f_n in the case of spFEM, and only 50% of calculated natural frequencies f_n in the case of FEM. Similar results are obtained, when the reduction in the bar cross-section is accompanied by a simultaneous reduction in the elastic modulus, also to 25% of its original value. The results of numerical computations for the same two modelling approaches are presented in Fig. 20. It should be mentioned here that due to the lack of known analytical solutions, as reference solutions the authors used FEM solutions, noted as FEM$^\infty$. They were obtained for rich FE discrete numerical models of the bar consisting 10 times more DOFs than the spFEM and FEM models under investigation.

The following examples of numerical computations aim to illustrate the ability of the current spFEM approach in modelling fatigue cracks or pin joints. At the beginning the influence of the relative crack depth a/R, in the case of an open transverse fatigue crack, on non-dimensional compliance $\tilde{c}_{11}$ and $\tilde{c}_{55}$ was investigated, as presented in Fig. 21 (left). Their values can be easily calculated according to formulas presented in [36–38] also for other types of fatigue cracks (internal, penny-shaped, circumferential, etc.). It should be added that the non-dimensional compliance $\tilde{c}_{11}$ is related to the loss of longitudinal stiffness of the bar due to the crack presence, while the non-dimensional compliance $\tilde{c}_{55}$ to the loss of flexural stiffness.

It is clearly seen from Fig. 21 that the use of the compatibility conditions expressed by Eq. (21) leads, as predicted, to a visible displacement jumps in selected longitudinal modes of natural vibrations of the bar as well as a decrease in associated natural frequencies. This is well illustrated in the case of the fundamental $\mathbf{q}_1$ (middle) and the third $\mathbf{q}_3$ (right) modes. The amplitudes of these jumps are not only a function of

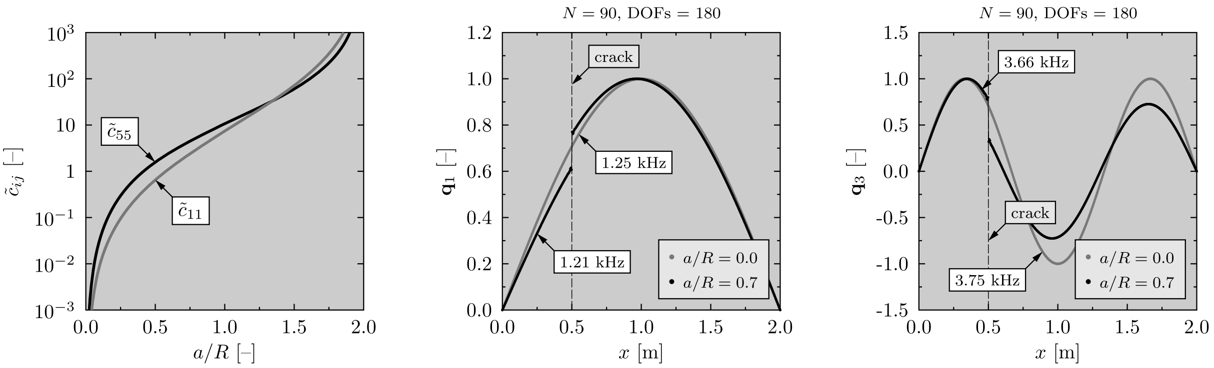

Fig. 21. Non-dimensional compliance $\tilde{c}_{11}$ and $\tilde{c}_{55}$ due to an open traverse fatigue crack [36,37], for longitudinal and flexural behaviour, as a function of the relative crack depth a/R (left). The influence of the crack on the fundamental $\mathbf{q}_1$ (middle) and the third $\mathbf{q}_3$ (right) longitudinal modes of natural vibrations of a 1-D aluminium cracked bar, associated with displacement nodal DOFs, for the crack located at one-quarter of the bar length. Numerical results obtained by the use of spFEM, according to the classical rod theory in the case of the bar of fixed ends, modelled by $N = 90$ spFEM (DOFs = 180) and approximation polynomials of degree $p = 2$.

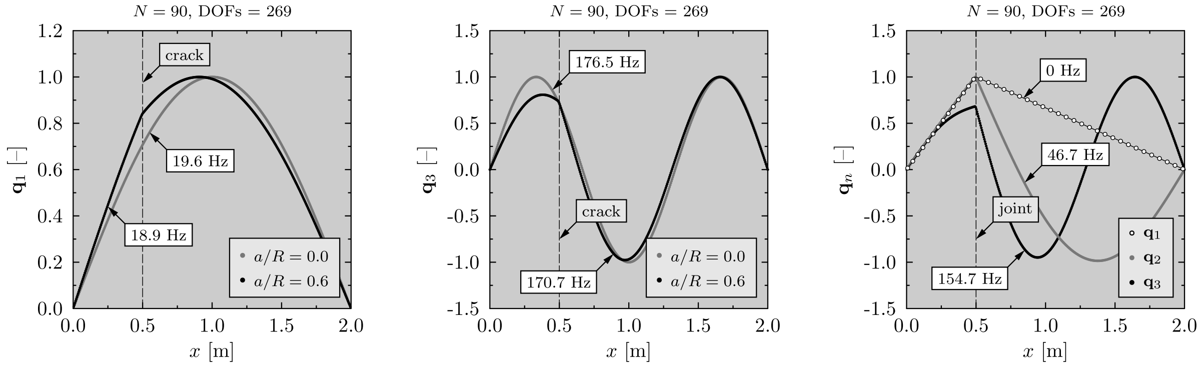

Fig. 22. The influence of the crack on the fundamental $\mathbf{q}_1$ (left) and the third $\mathbf{q}_3$ (middle) flexural modes of natural vibrations of a 1-D aluminium cracked bar, associated with displacement nodal DOFs, for the crack located at one-quarter of the bar length. First three flexural modes of natural vibrations of a pin-joined bar (right). Numerical results obtained by the use of spFEM, according to the classical beam theory in the case of the bar of simply-supported ends, modelled by $N = 90$ spFEM (DOFs = 269) and approximation polynomials of degree $p = 3$.

the mode number n, but primarily a function of the relative crack depth a/R. In the cases, when the position of the crack coincides with a modal node, as is for the second mode of natural vibrations, the presence of the crack has no influence on this mode.

In a similar manner the use of the compatibility conditions expressed by Eq. (22) leads, as predicted, to a visible jumps in selected flexural modes of natural vibrations of the bar as well as a decrease in associated natural frequencies, as shown in Fig. 22. In these cases, however, the jumps concern not displacements, but their spatial derivatives, i.e. rotations. Again, this is well illustrated in the case of the fundamental $\mathbf{q}_1$ (left) and the third $\mathbf{q}_3$ (middle) modes. In this case it is interesting to see that when the relative depth of the crack a/R tends to 2, which corresponds to the total loss of the flexural stiffness in the crack position, the observed behaviour of the bar full corresponds to the behaviour of the bar with a pin joint. In the regime of lower natural frequencies the obtained results in the case of the pin joint modelled by separation of appropriate rotational DOFs, or simulated by an extreme case of the transverse fatigue crack, are practically the same (right).

It should be added here that the modes of natural vibrations shown in Fig. 21 and Fig. 22 are associated only with displacement DOFs and similar graphs can be obtained for all remaining DOFs representing their higher order spatial derivatives. Moreover, the results of numerical computations presented in Fig. 21 and Fig. 22 have no corresponding reference solutions due to many various procedures available in the literature, which can be used to calculate the values of the non-dimensional compliance $\tilde{c}_{11}$ and $\tilde{c}_{55}$, and which would lead to slightly different results. If necessary FE discrete numerical models can be individually tuned in this respect to fit either experimental data or results of full 3-D analysis.

6. Conclusions

In this paper a computational methodology leading to the development of a new class of 1-D FEs, based on the application of continuous and smooth approximation polynomials being spline functions, has been presented. Application of splines as appropriately defined piecewise elemental shape functions led the authors to the formulation of a new approach for FEM, named as spFEM, where in contrast to the well-known NURBS approach, the boundaries of spFEs are well-defined, exactly as it is in the case of the traditional FEM. The current numerical approach has been computationally verified by the authors it terms of dynamic problems including: spectra of natural frequencies, mode of natural vibrations and wave propagation problems, especially in the aspect of high frequency dynamics in the case of selected one- and two-mode theories of 1-D structural elements. The applicability of the proposed approach has been evaluated and compared, in terms of calculated dynamic responses, with the results obtained by the use of other well-established FEM approaches.

It has been found that the well-establishes FEM approaches suffer from a problem associated with the discontinuity of the stress/strain fields between adjacent FEs, which in the case of high frequency dynamics may lead to serious numerical problems resulting from the periodic nature of FE discrete numerical models, typical for these approaches. The key feature of the periodicity of such FE discrete numerical models is the presence of frequency band gaps in calculated spectra of natural frequencies, which most prominently manifest themselves in the regime of high frequencies. For this reason the periodic nature of FE models is most strongly revealed just in the case of problems related to wave propagation, as associated with high frequency dynamic responses, where regular and dense meshes of FEs are required for computations to guarantee high accuracy of the results of numerical computations.

It turns out that in the worst cases even relatively rich FE discrete numerical models of many DOFs may lead to wrong or falsified results. This is also applicable to the approaches that are traditionally associated with wave propagation problems, as is TD-SFEM. In all such and similar cases a careful initial analysis should be performed in order to ensure that sought dynamic responses remain unaffected. This can be achieved by the use of the Bloch theorem, as demonstrated and presented in the current work.

In all cases analysed by the authors the proposed spFEM turned out to be the most accurate approach. What is more spFEM proved to be free from the main drawback of the other tested FEM approaches, thanks to the class of differentiability of approximation polynomials, which guarantees the absence of any frequency band gaps in calculated spectra of natural frequencies. On the other hand, a direct consequence of this feature of spFEM is that a relatively large part of calculated spectra of natural frequencies, the same as modes of natural vibrations, can effectively be used for calculation of dynamic reposes even in the case of multi-mode theories. This has been also shown in the paper.

The numerical studies carried out by the authors concerned dynamic responses of simple 1-D structural elements. Despite this fact the conclusions presented below remain valid also for other types of structural elements. They are also applicable to 2-D and 3-D structural elements of complex geometries and material properties as long as their discrete numerical representations have the features typical of periodic structures, i.e. which are characterised by large numbers of FEs of the same or similar sizes, which is common in the case of wave propagation analysis.

The above statements can be summarised in the following way:

- FE discrete numerical models may be thought of as representing periodic structures.
- The periodic nature of these FE models results from the discontinuity of the stress/strain fields between adjacent FEs.
- The periodicity of FE models manifests itself as the presence of frequency band gaps in calculated spectra of natural frequencies.
- The presence of these frequency band gaps substantially limits the usable part of calculated spectra of natural frequencies and may falsify calculated dynamic responses, especially in the high frequency regimes.
- The number of frequency band gaps is directly correlated with the degree of approximation polynomials and the level of their differentiability.
- Thanks to the appropriately defined approximation polynomials, as are piecewise splines, the current spFEM approach shows no periodic features.
- Out of the three FEM approaches tested, these being: FEM, TD-SFEM and spFEM, only the current spFEM approach is characterised by the greatest accuracy measured in terms of the agreement with analytical results within the greatest part of the calculated spectrum of natural frequencies.
- It has been also demonstrated that thanks to its formulation spFEM approach poses extra modelling features, which makes its applicable for the problems involving modelling of structural discontinuities as fatigue cracks, step changes in geometrical and/or material properties, or structural joints.
- In all relevant cases, except these concerning extra modelling features, the results of numerical computations obtained by the use of the current formulation of spFEM fully agreed with those obtained by the use of B-splines, as presented in [11].

Acknowledgements

The authors of this work would like to gratefully acknowledge the support for their research provided by the Academic Computer Centre in Gdańsk. All results presented in this paper have been obtained by the use of the software available at the Academic Computer Centre in Gdańsk.

Appendix A. Bloch theorem

The Bloch theorem enables one to transform a solution to the wave equation from the level of the entire periodic structure to the level of a single cell representing this structure. In a 1-D case the Bloch theorem can be express by a simple equation, which states that the sought solution $\psi(x)$, also known as the Bloch wave, can be represented as a combination of a harmonic wave e^{ikx} and a certain periodic function $u(x)$ of the same periodicity as the periodicity of the structure as:

$$\psi(x) = e^{ikx}u(x) \tag{A.1}$$

where k is the wave number, i is the imaginary unit, i.e. $i^2 = -1$, while x denotes a spatial co-ordinate. Under the assumption that the entire structure consists of N cells of length l the Bloch theorem states that the Bloch wave $\psi(x)$ has the following property:

$$\psi(x+l) = e^{ik(x+l)}u(x+l) = e^{ikl}e^{ikx}u(x+a) = e^{ikl}e^{ikx}u(x) = e^{ikl}\psi(x) \tag{A.2}$$

since $u(x+a) = u(x)$ has the same periodicity as the structure.

Taking into account N cells and noting that the total length of the entire periodic structure is equal to $L = l \cdot N$, it can be written that:

$$\psi(x) = \psi(x+L) = \psi(x + l\cdot N) = e^{iklN}\psi(x) \tag{A.3}$$

which is satisfied only if $e^{iklN} = 1$. This enables one to express the wave number k associated with the harmonic wave e^{ikx} as:

$$e^{iklN} = e^{i2\pi n} \quad \rightarrow \quad k_n = \frac{2\pi n}{lN}, \quad n = 0, 1, \dots, N \tag{A.4}$$

which on the other hand helps to express the Bloch wave in its final form as:

$$\psi(x+l) = e^{i\frac{2\pi n}{N}}\psi(x) \tag{A.5}$$

This final form of the Bloch wave states that the wave motion of the whole periodic structure can be successfully described from the level of a single cell of this structure, since a simple shift in the argument in the Bloch wave $\psi(x+l)$ allows one to describe the wave motion of all adjacent cells by the very same wave itself, i.e. by $\psi(x)$. In this manner the analysis of the wave motion or natural frequency spectra can be carried out from the level of a single cell of the structure, but for a sequence of the wave numbers k_n, with $n = 0, 1, \dots, N$. This corresponds to the representation of the results of such analysis within the so-called reduced (first or Brillouin) zone of the reciprocal space [25–27] of the wave vector k.

However, thanks to the Bloch theorem these results can also be easily extended onto the entire reciprocal space of the wave vector k, which then is associated with the total length of the periodic structure L rather than the length of a single cell of this structure l.

Appendix B. Bloch reduction

The Bloch reduction technique may be understood as a numerical implementation of the Bloch theorem. In a general case of a 1-D rod modelled by FEM, the analysis of its natural frequency spectrum requires solution of a well-known eigenvalue problem:

$$(\mathbf{K} - \omega^2\mathbf{M})\cdot\mathbf{q} = \mathbf{0} \tag{B.1}$$

which in the case of the Bloch theorem can be formulated at the level of a single rod FE rather than the entire rod modelled by a number of

FEs. For this reason the symbols **K** and **M** denote the elemental stiffness and inertia matrices, while **q** is a vector of nodal displacements with **0** being a null vector.

It should be noted that the nodal displacements of the rod FE having m nodes may be conveniently divided into a group of internal nodal displacements $q_i (i = 2, \dots, m-1)$ and a group of boundary nodal displacements $q_i (i = 1, m)$.

Application of the Bloch theorem to the boundary nodal displacements $q_i (i = 1, m)$ allows one to write that:

$$q_m = q_1 e^{i\frac{2\pi n}{N}}, \quad n = 0, 1, \dots, N \tag{B.2}$$

where N is equal to the total number of FEs modelling the rod.

In this manner the original eigenvalue problem given by Eq. (B.1) can be reduced to a new eigenvalue problem:

$$\left[\mathbf{K}_r(n) - \omega^2 \mathbf{M}_r(n)\right] \cdot \mathbf{q}_r(n) = \mathbf{0} \tag{B.3}$$

where the reduced elemental stiffness $\mathbf{K}_r(n)$ and inertia $\mathbf{M}_r(n)$ matrices are expressed as:

$$\begin{cases} \mathbf{K}_r(n) = \mathbf{A}(n)^\intercal \cdot \mathbf{K} \cdot \mathbf{A}(n) \\ \mathbf{M}_r(n) = \mathbf{A}(n)^\intercal \cdot \mathbf{M} \cdot \mathbf{A}(n) \end{cases} \tag{B.4}$$

with the rectangular matrix $\mathbf{A}(n)$ of size $m \times (m-1)$ defined in the following manner:

$$\begin{cases} A_{j,j} = 1, & j = 1, 2, \dots, m-1 \\ A_{j,1} = e^{i\frac{2\pi n}{N}}, & j = m \end{cases} \tag{B.5}$$

The general procedure described above can be successfully modified and employed also for other types of 1-D FEs, including various rod, beam or bar theories, as presented by the authors [11,12,28]. It should be noted that in such cases the Bloch reduction technique must concern all available nodal DOFs of boundary nodes.

Appendix C. Classical rod theory

The simplest theory that can be employed to study the longitudinal behaviour of 1-D structures is the classical rod theory. In this theory, under the assumption of small displacements and small strains, the displacement field within a 1-D rod has only one non-zero axial displacement component u_x, which can be expressed by the function $u(x)$. In the cylindrical co-ordinate system $xr\phi$ it can be formally written that [26]:

$$u_x(x, r, \phi) = u(x) \tag{C.1}$$

while the remaining radial and tangential displacement components u_r and u_ϕ vanish.

As a consequence of this the strain field has also only one non-zero strain component, which is the axial strain ϵ_{xx}:

$$\epsilon_{xx}(x, r, \phi) = \frac{\partial u(x)}{\partial x} \tag{C.2}$$

The knowledge of the displacement field and the strain field allows one to build the characteristic stiffness **K** and inertia **M** matrices for various FEs based on the classical rod theory. This can be easily done by the use of the well-known FEM procedures [5–7] as soon as the function $u(x)$ is replaced by a set of approximating shape functions, which definitions depend on the number of nodes of the FEs.

Additionally, based on the assumed forms of the displacement field and the strain field the strain energy and the kinetic energy can be easily evaluated and associated with the longitudinal wave motion. Next, by the use of Hamilton's principle the equation of motion associated with the longitudinal behaviour of the rod can be easily obtained [26] as:

$$ES \frac{\partial^2 u(x)}{\partial x^2} = \rho S \frac{\partial^2 u(x)}{\partial t^2} \tag{C.3}$$

where E is Young's modulus of the rod material, S is the area of rod cross-section, ρ is the material density, while t denotes time.

The equation of motion given by Eq. (C.3) comes as very useful for obtaining the dispersion curve associated with the classical rod theory [26]. This can be easily achieved under the assumption that solution to this equation of motion has the form of a harmonic wave, i.e. when $u_x(x,t) = \hat{u}_x e^{i(kx-\omega t)}$, where $\hat{u}_x$ is the amplitude of this harmonic wave, while ω is its angular frequency.

Finally, it can be found that the phase velocity c_p of the longitudinal waves associated with the longitudinal behaviour of the classical rod under consideration can be expressed by a very well-know dispersion relation:

$$c_p = \frac{\omega}{k} = \sqrt{\frac{E}{\rho}} \tag{C.4}$$

Appendix D. Bernoulli-Euler beam theory

The simplest theory that can be employed to study the flexural (bending) behaviour of 1-D structures is the Bernoulli-Euler beam theory. In this theory, under the assumption of small displacements and small strains, the displacement field within a 1-D beam has three displacement components: axial u_x, radial u_r and tangential u_ϕ, which can be expressed by one independent function $w(x)$. It should be noted that this form of the displacement field results from an additional assumption of vanishing transverse shear strains within the beam, which is true for thin beams, when the length-to-thickness ratio is of the order of 20 or more, or beams subjected to low frequency excitations. Thus, in the cylindrical co-ordinate system $xr\phi$ in can be formally written that [30]:

$$\begin{cases} u_x(x, r, \phi) = -r \dfrac{\partial w(x)}{\partial x} \sin\phi \\ u_r(x, r, \phi) = w(x) \sin\phi \\ u_\phi(x, r, \phi) = w(x) \cos\phi \end{cases} \tag{D.1}$$

The resulting strain field has also only one non-zero strain component, which is the axial strain ϵ_{xx}:

$$\epsilon_{xx}(x, r, \phi) = -r \frac{\partial^2 w(x)}{\partial x^2} \tag{D.2}$$

The knowledge of the displacement field and the strain field allows one to build the characteristic stiffness **K** and inertia **M** matrices for various FEs based on the Bernoulli-Euler beam theory. This can be easily done by the use of the well-known FEM procedures [5–7] as soon as the function $w(x)$ is replaced by a set of approximating shape functions, which definitions depend on the number of nodes of the FEs.

Based on the assumed forms of the displacement field and the strain field the strain energy and the kinetic energy can be easily evaluated and associated with the flexural (bending) wave motion. Next, by the use of Hamilton's principle the equation of motion associated with the flexural (bending) behaviour of the beam can be easily obtained [30] as:

$$EI \frac{\partial^4 w(x)}{\partial x^4} = -\rho S \frac{\partial^2 w(x)}{\partial t^2} + \rho I \frac{\partial^4 w(x)}{\partial x^2 \partial t^2} \tag{D.3}$$

where E is Young's modulus of the beam material, S and I are the area and the second moment of area of the beam cross-section, ρ is the material density, while t denotes time. It should be mentioned here that very often the inertial part of the equation of motion given by Eq. (D.3), proportional to ρI, is neglected as having very small influence in the case of thin beams, i.e. when the assumptions of the Bernoulli-Euler beam theory are satisfied.

The equation of motion given by Eq. (D.3) comes as very useful for obtaining the dispersion curve associated with the Bernoulli-Euler beam theory [30]. This can be easily achieved under the assumption that solution to this equation of motion has the form of a harmonic wave, i.e. when $w(x,t) = \hat{w}e^{i(kx-\omega t)}$, where $\hat{w}$ is the amplitude of this harmonic wave, while ω is its angular frequency.

Finally, it can be found that the phase velocity c_p of the flexural (bending) waves associated with the flexural (bending) behaviour of the Bernoulli-Euler beam under consideration can be expressed by a very well-know dispersion relation:

$$c_p = \frac{\omega}{k} = \sqrt[4]{\frac{EI}{\rho S}}\sqrt{\omega} \tag{D.4}$$

Appendix E. Timoshenko beam theory

An advanced theory that can be employed to study the flexural (bending) behaviour of 1-D structures is the Timoshenko beam theory. In this theory, under the assumption of small displacements and small strains, the displacement field within a 1-D beam has three non-zero displacement components: axial u_x, radial u_r and tangential u_ϕ, which can be expressed by two independent functions $u(x)$ and $w(x)$. In the case of the Timoshenko beam theory transverse shear strains do not vanish, which is true for thick beams or beams subjected to high frequency excitations. Thus, in the cylindrical co-ordinate system $xr\phi$ in can be formally written that [30]:

$$\begin{cases} u_x(x,r,\phi) = ru(x)\sin\phi \\ u_r(x,r,\phi) = w(x)\sin\phi \\ u_\phi(x,r,\phi) = w(x)\cos\phi \end{cases} \tag{E.1}$$

The resulting strain field has three non-zero strain components, which are the axial strain ϵ_{xx} and two shear strains γ_{xr} and $\gamma_{x\phi}$:

$$\begin{cases} \epsilon_{xx}(x,r,\phi) = r\dfrac{\partial u(x)}{\partial x}\sin\phi \\ \gamma_{xr}(x,r,\phi) = \left[u(x) + \dfrac{\partial w(x)}{\partial x}\right]\sin\phi \\ \gamma_{x\phi}(x,r,\phi) = \left[u(x) + \dfrac{\partial w(x)}{\partial x}\right]\cos\phi \end{cases} \tag{E.2}$$

The knowledge of the displacement field and the strain field allows one to build the characteristic stiffness **K** and inertia **M** matrices for various FEs based on the Timoshenko beam theory. This can be easily done by the use of the well-known FEM procedures [5–7] as soon as the functions $u(x)$ and $w(x)$ are replaced by sets of approximating shape functions, which definitions depend on the number of nodes of the FEs.

Based on the assumed forms of the displacement field and the strain field the strain energy and the kinetic energy can be easily evaluated and associated with the flexural (bending) wave motion. Next, by the use of Hamilton's principle the equations of motion associated with the flexural (bending) behaviour of the Timoshenko beam can be easily obtained [30] as:

$$\begin{cases} EI\dfrac{\partial^2 u(x)}{\partial x^2} - SG\kappa\left[u(x) + \dfrac{\partial w(x)}{\partial x}\right] = \rho I\dfrac{\partial^2 u(x)}{\partial t^2} \\ SG\kappa\left[u(x) + \dfrac{\partial w(x)}{\partial x}\right] = \rho S\dfrac{\partial^2 w(x)}{\partial t^2} \end{cases} \tag{E.3}$$

where E is Young's modulus of the beam material, S and I are the area and the second moment of area of the beam cross-section, κ is a shear coefficient, ρ is the material density, while t denotes time.

The equations of motion given by Eq. (E.3) come as very useful for obtaining the dispersion curves associated with the Timoshenko beam theory [30]. This can be easily achieved under the assumption that solution to this equation of motion has the form of two independent harmonic waves, i.e. when $u(x,t) = \hat{u}e^{i(kx-\omega t)}$ and $w(x,t) = \hat{w}e^{i(kx-\omega t)}$, where $\hat{u}$ and $\hat{w}$ denote the amplitudes of $u(x,t)$ and $w(x,t)$, while ω is the angular frequency.

Finally, it can be found that the phase velocities c_p of two independent modes of flexural (bending) and shear waves associated with the flexural (bending) behaviour of the Timoshenko beam under consideration can be expressed based on the following dispersion relation:

$$I(Ek^2 - \rho\omega^2)(\kappa Gk^2 - \rho\omega^2) - \kappa GS\rho\omega^2 = 0 \rightarrow k = k(\omega) \rightarrow c_p = \frac{\omega}{k} \tag{E.4}$$

References

[1] W. Ostachowicz, P. Kudela, M. Krawczuk, A. Żak, Guided Waves in Structures for SHM. The Time-domain Spectral Element Method, John Wiley & Sons Ltd., Singapore, 2012.

[2] M. Mitra, S. Gopalakrishnan, Guided wave based structural health monitoring: a review, Smart Mater. Struct. 25 (2016) 1–28.

[3] S.W. Liu, J.H. Huang, J.C. Sung, C.C. Lee, Detection of cracks using neural networks and computational mechanics, Comput. Methods Appl. Mech. Eng. 191 (2002) 2831–2845.

[4] H. Peng, G. Meng, F. Li, Modeling of wave propagation in plate structures using three-dimensional spectral element method for damage detection, J. Sound Vib. 320 (2009) 942–954.

[5] J.T. Oden, J.N. Reddy, An Introduction to the Mathematical Theory of Finite Elements, Wiley, New York, 1976.

[6] O.C. Zienkiewicz, The Finite Element Method, McGraw–Hill Book Company, London, 1989.

[7] S.S. Rao, The Finite Element Method in Engineering, Pergamon Press, Oxford, 1981.

[8] I. Babuška, B.Q. Guo, The *h*, *p* and *h-p* version of the finite element method: basis theory and applications, Adv. Eng. Softw. 15 (1992) 159–192.

[9] M. Ainsworth, J.T. Oden, A Posteriori Error Estimation in Finite Element Analysis, John Wiley & Sons, Ltd., New York, 2011.

[10] C. Pozdrikidis, Introduction to Finite and Spectral Element Methods Using MATLAB, Chapman and Hall//CRC, Boca Raton, 2005.

[11] A. Żak, M. Krawczuk, M. Palacz, Periodic properties of 1D FE discrete models in high frequency dynamics, Math. Probl. Eng. (2016) 9651430, 1–15.

[12] A. Żak, M. Krawczuk, M. Palacz, Ł. Doliński, W. Waszkowiak, High frequency dynamics of an isotropic Timoshenko periodic beam by the use of the Time-domain Spectral Finite Element Method, J. Sound Vib. 409 (2017) 318–335.

[13] P.M. Prenter, Splines and Variational Methods, Dover Publications, Inc., New York, 1975.

[14] C. de Boor, A Practical Guide to Splines, Springer-Verlag New York Inc., New York, 1978.

[15] K. Höllig, Finite Element Methods with B-Splines, SIAM, Philadelphia, 2003.

[16] D.F. Rogers, An Introduction to NURBS: With Historical Perspective, Morgan Kauffmann Publishers, San Francisco, 2000.

[17] T.J.R. Hughes, J.A. Cottrell, Y. Bazilevs, Isogeometric analysis: CAD, finite elements, NURBS, exact geometry and mesh refinement, Comput. Methods Appl. Mech. Eng. 194 (2005) 4135–4195.

[18] J.A. Cottrell, T.J.R. Hughes, Y. Bazilevs, Isogeometric Analysis: Toward Integration of CAD and FEA, John Wiley & Sons Ltd., Singapore, 2009.

[19] W. Ostachowicz, M. Krawczuk, Modeling for detection of degraded zones in metallic and composite structures, in: Encyclopedia of Structural Health Monitoring, John Wiley & Sons Ltd., Chichester, 2009, pp. 851–866.

[20] A.A. Shabana, A.M. Hamed, A.-N.A. Mohamed, P. Jayakumar, M.D. Letherwood, Limitations of B-spline geometry in the finite element/multibody system analysis, in: Proceedings of the 8th International Conference on Multibody Systems, Nonlinear Dynamics, and Control, Parts A and B, vol. 4, 2011, pp. 861–871.

[21] K. Höllig, U. Reif, J. Wipper, Weighted extended B-spline approximation of Dirichlet problems, SIAM J. Numer. Anal. 39 (2001) 442–462.

[22] L. Shen, Z. Liu, J.H. Wu, B-spline finite element method based on node moving adaptive refinement strategy, Finite Elem. Anal. Des. 91 (2014) 84–94.

[23] A. Chakraborty, B.V.R. Kumar, Weighted extended B-spline finite element analysis of a coupled system of general elliptic equations, Int. J. Adv. Eng. Sci. Appl. Math. 10 (2018) 34–40.

[24] A. Żak, M. Krawczuk, Certain numerical issues of wave propagation modelling in rods by the Spectral Finite Element Method, Finite Elem. Anal. Des. 47 (2011) 1036–1046.

[25] L. Brillouin, Wave Propagation in Periodic Structures, Electric Filters and Crystal Latices, Dover Publications, Inc., New York, 1946.

[26] A. Żak, M. Krawczuk, Assessment of rod behaviour theories used in spectral finite element modelling, J. Sound Vib. 329 (2010) 2099–2113.

[27] C. Kittel, Introduction to Solid State Physics, John Wiley & Sons, Inc., New York, 2005.

[28] A. Żak, M. Krawczuk, G. Redlarski, Ł. Doliński, S. Koziel, A three-dimensional periodic beam for vibroacoustic isolation purposes, Mech. Syst. Signal Process. 130 (2019) 524–544.

[29] D. Duhamel, B.R. Mace, M.J. Brennan, Finite element analysis of the vibrations of waveguides and periodic structures, J. Sound Vib. 294 (2006) 205–220.

[30] A. Żak, M. Krawczuk, Assessment of flexural beam behaviour theories used for dynamics and wave propagation problems, J. Sound Vib. 331 (2012) 5715–5731.

[31] A. Ralston, P. Rabinowitz, A First Course in Numerical Analysis, Dover Publications, Inc., New York, 2001.

[32] A. Asmus, R. Lammering, Actual time integration methods for elastic wave propagation analysis, Proc. Appl. Math. Mech. 14 (2014) 857–858.

[33] http://www.mathworks.com/.

[34] J.L. Rose, Ultrasonic Waves in Solid Media, Cambridge University Press, Cambridge, 1999.

[35] J.D. Achenbach, Wave Propagation in Elastic Solids, North-Holland Publishing Company, Amsterdam, 1973.

[36] C.A. Papadopoulos, A.D. Dimarogonas, Coupled longitudinal and bending vibrations of a rotating shaft with an open crack, J. Sound Vib. 117 (1987) 81–93.

[37] G. Bao, S. Ho, Z. Suo, B. Fan, The role of material orthotropy in fracture specimens for composite, Int. J. Solids Struct. 29 (1992) 1105–1116.

[38] M. Krawczuk, M. Palacz, W. Ostachowicz, The dynamic analysis of a cracked Timoshenko beam by the spectral element method, J. Sound Vib. 264 (2003) 1139–1153.